Thermal anomalies in Central Elysium Planitia and Arsia Mons.
Evidence and implications of aerothermal systems

Téodolina LOPEZ
PhD Advisors : David Baratoux
Michel Rabinowicz

Seminar in Kobe Institute
12/10/2009

A new word

Hydrothermal system → Water

Aerothermal system → Air

Contents

Location of Formica Léo

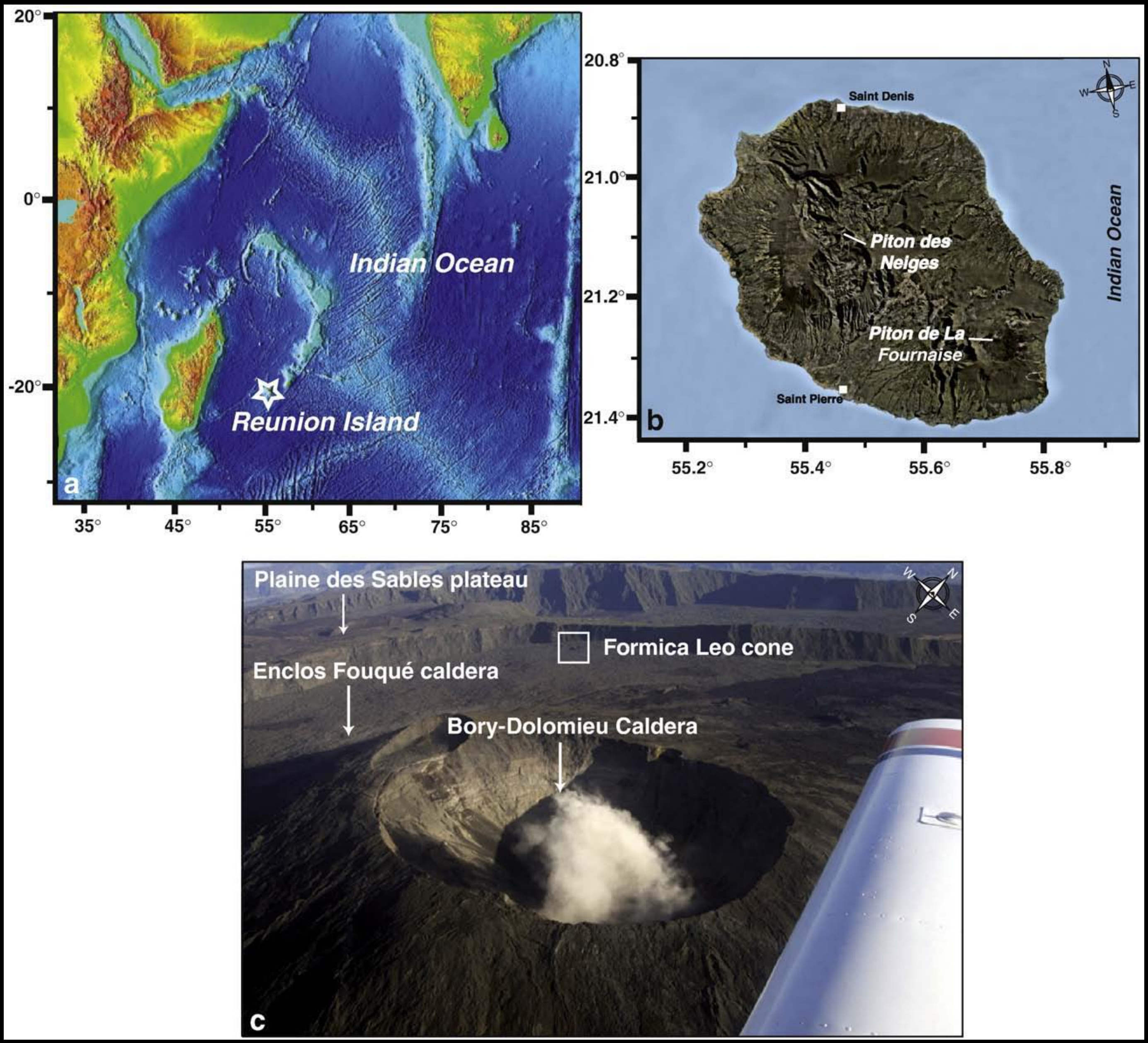

Antoine et al., JVGR 2009

Formica Léo

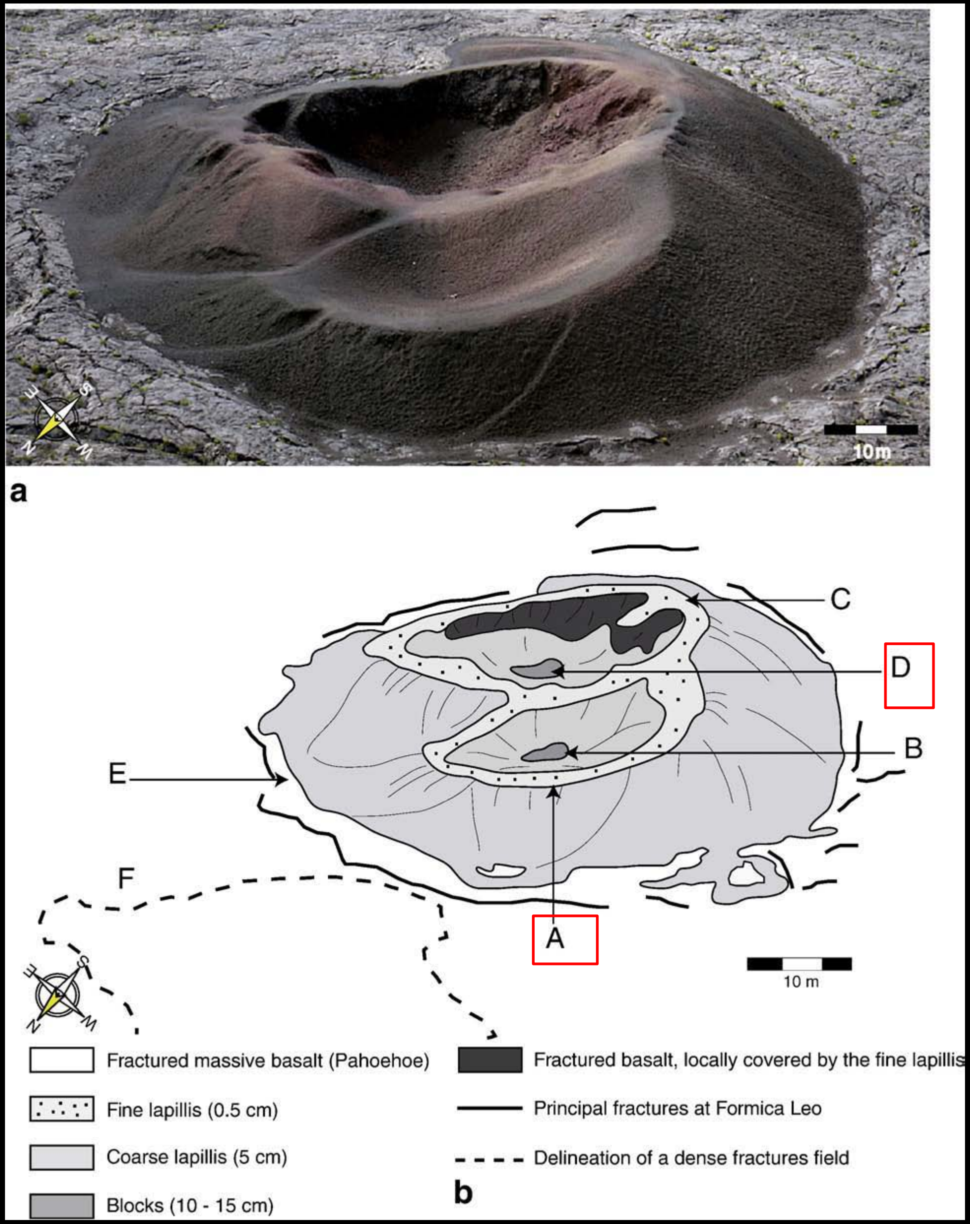

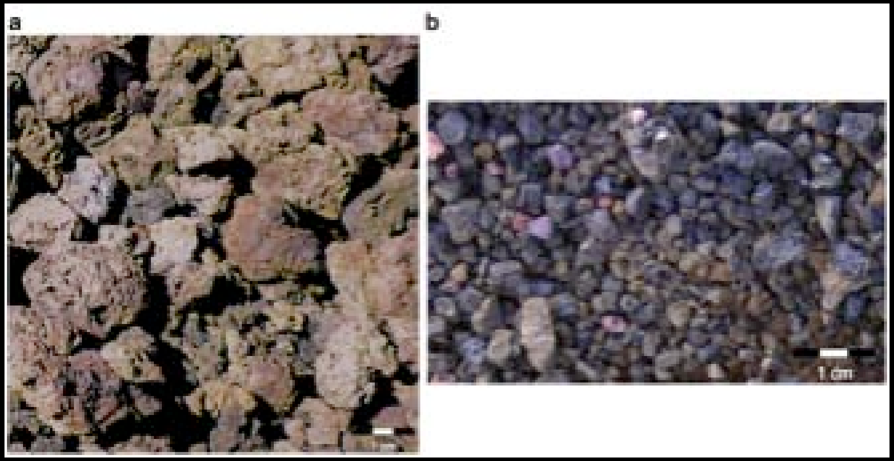

a) Blocks : bottom SE crater (A)
b) Fine lapillis: top of Formica Leo (D)

Picture of Formica Léo with the classes material location.

Antoine et al., JVGR 2009

Thermal study

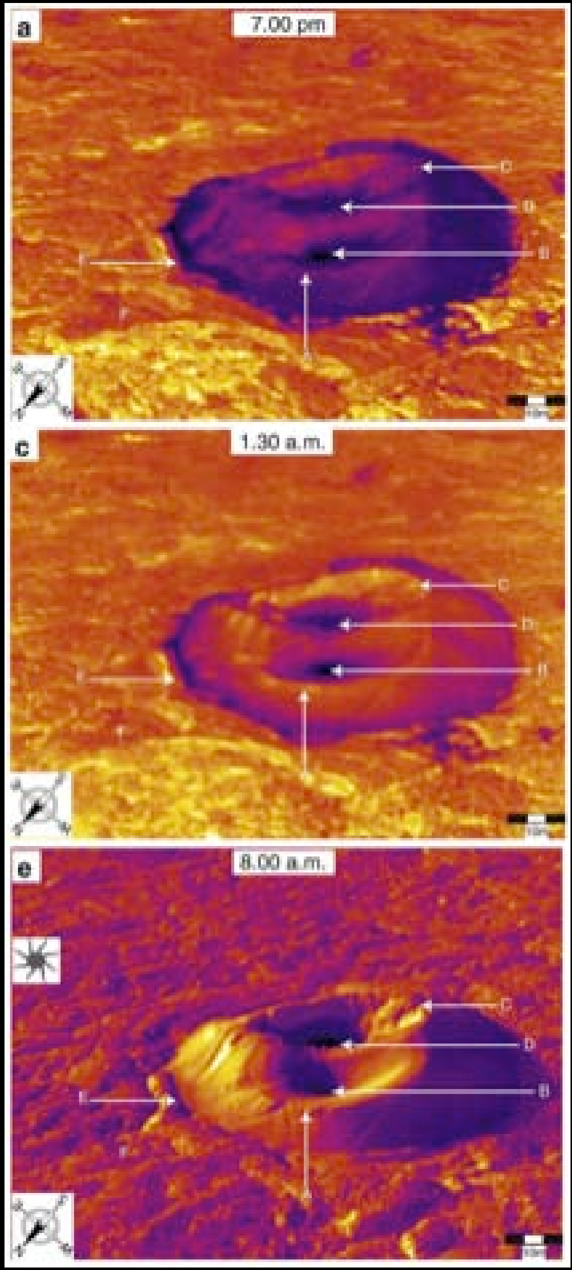

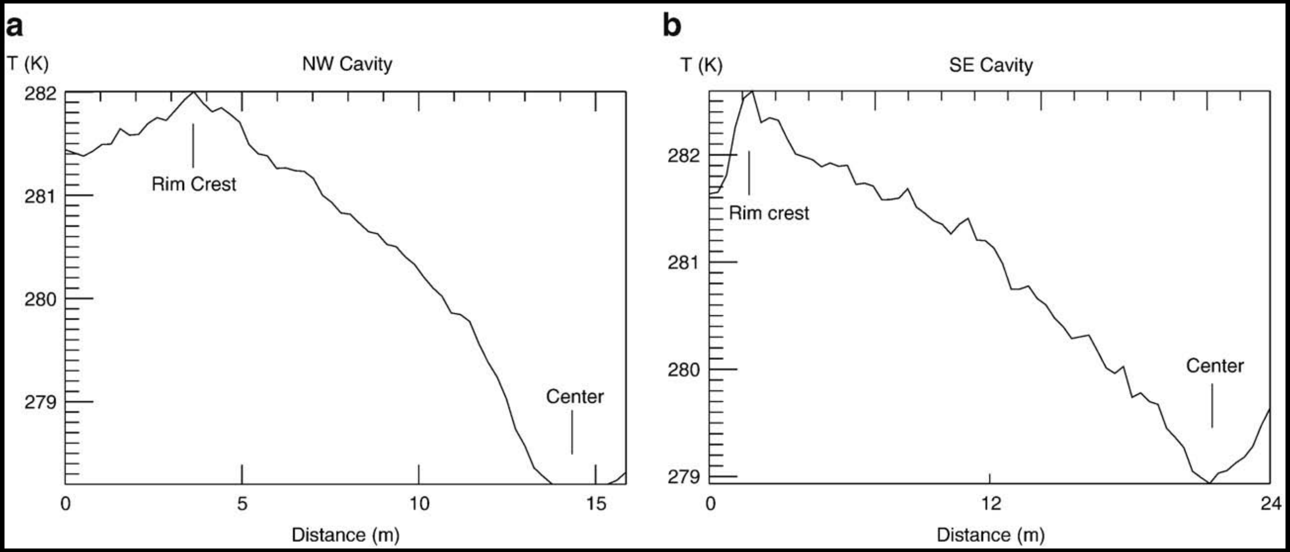

Midnight surface temperature profiles of the two craters. A drop of about 3K is observed from the rim crest to the crater center.

Thermal images of Formica Léo during night. Craters bottom are cold while the rim crests are warm.

Antoine et al., JVGR 2009

Thermal conductivity

- Definition : It is the property of a material that indicates its ability to conduct heat. It is expressed in Watt/Kelvin/meters.

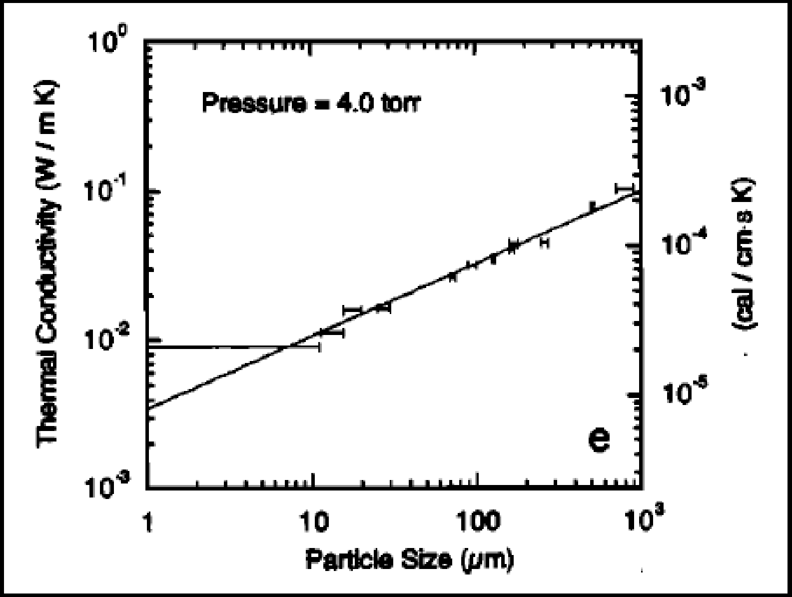

Presley and Christensen (1997) have shown that thermal conductivity increases with increasing particle size and atmospheric pressure.

Piqueux and Christensen (2009) : Their thermal model reproduces the thermal conductivity dependency of a sample with grain size and pressure and also confirms that higher porosities generally lead to lower conductivities.

2D Numerical model _ Presentation

Antoine et al., JVGR 2009

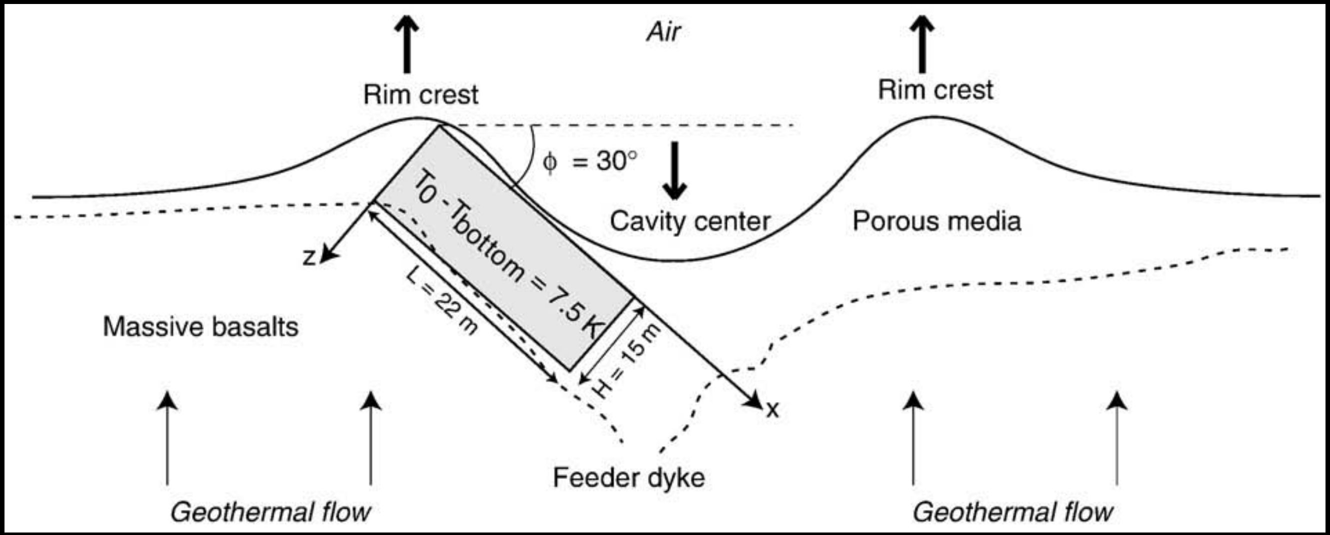

Representation of the box used for the air convection model.

Equations of the model:

$$\boxed{Ra = \rho_a\, g\, \alpha\, \Delta T\, H\, K / \mu\, \kappa}$$

$$\boxed{Ra_{eq} = \gamma\, Ra}$$

Height of the box	H	15 m
Length of the box	L	22 m
Slope of the box	⊠	30°
Heat capacity of the air	C_a	1000 J kg^{-1} K^{-1}
Air density	ρ_a	1 kg m^{-3}
Air thermal expansion	α	3.7×10^{-3} K^{-1}
Air Viscosity	μ	1.5×10^{-5} Pa s
Air–soil volumic heat capacity ratio	γ	5.0×10^{-4}
Permeability of the soil	K	3×10^{-8}–10^{-5} m^2
Thermal conductivity of the soil	k	0.4 W m^{-1} K^{-1}
Porosity of the soil	n	0.4
Top to bottom temperature contrast	ΔT	7.5 K
Phase shift	ζ	0
Pulsation scale	Ω	45,507 s
Darcy velocity scale	v	2.7×10^{-5} m s^{-1}
Geothermal heat flux(for k = 2.5)		1250 mW m^{-2}
Equivalent Rayleigh number	Ra_{eq}	20.4–6800

Notation and values used for the model

2D Numerical model _ Results

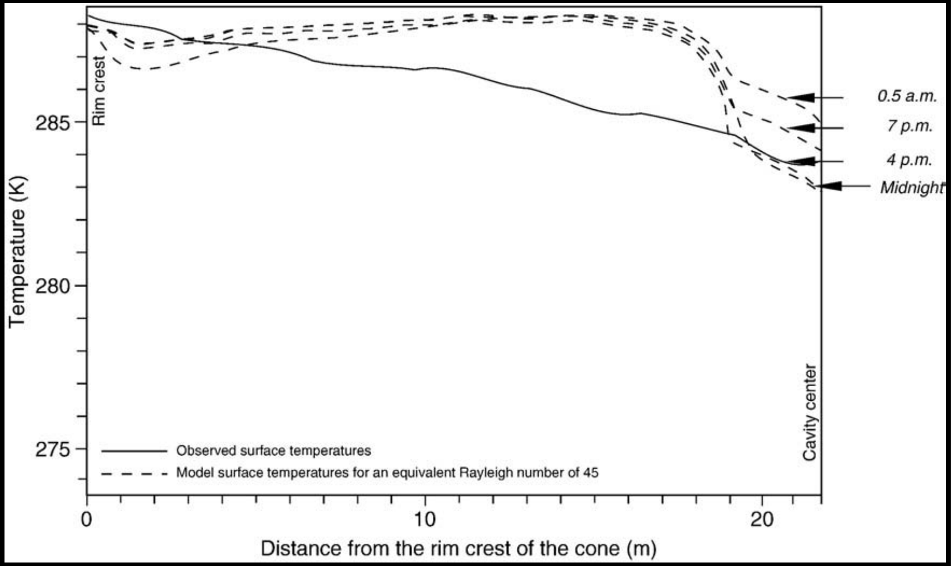

a) Surfaces temperatures calculated at different times for a Ra_{eq} = 45 (dotted lines). Explains the observed rim crest to crater center temperature drop.

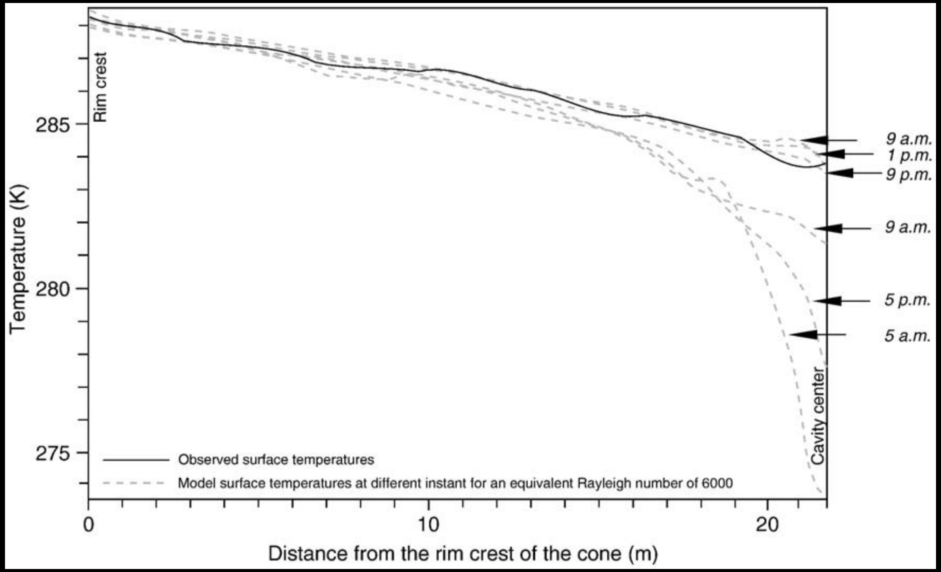

b) Surfaces temperatures calculated at different times for a Ra_{eq} = 6000 (dotted lines). Fit the observed temperature shape, while its amplitude is twice as large.

Air convection within the craters can explain the observed temperature pattern.

Antoine et al., JVGR 2009

Measurements of Spontaneous Potential (SP)

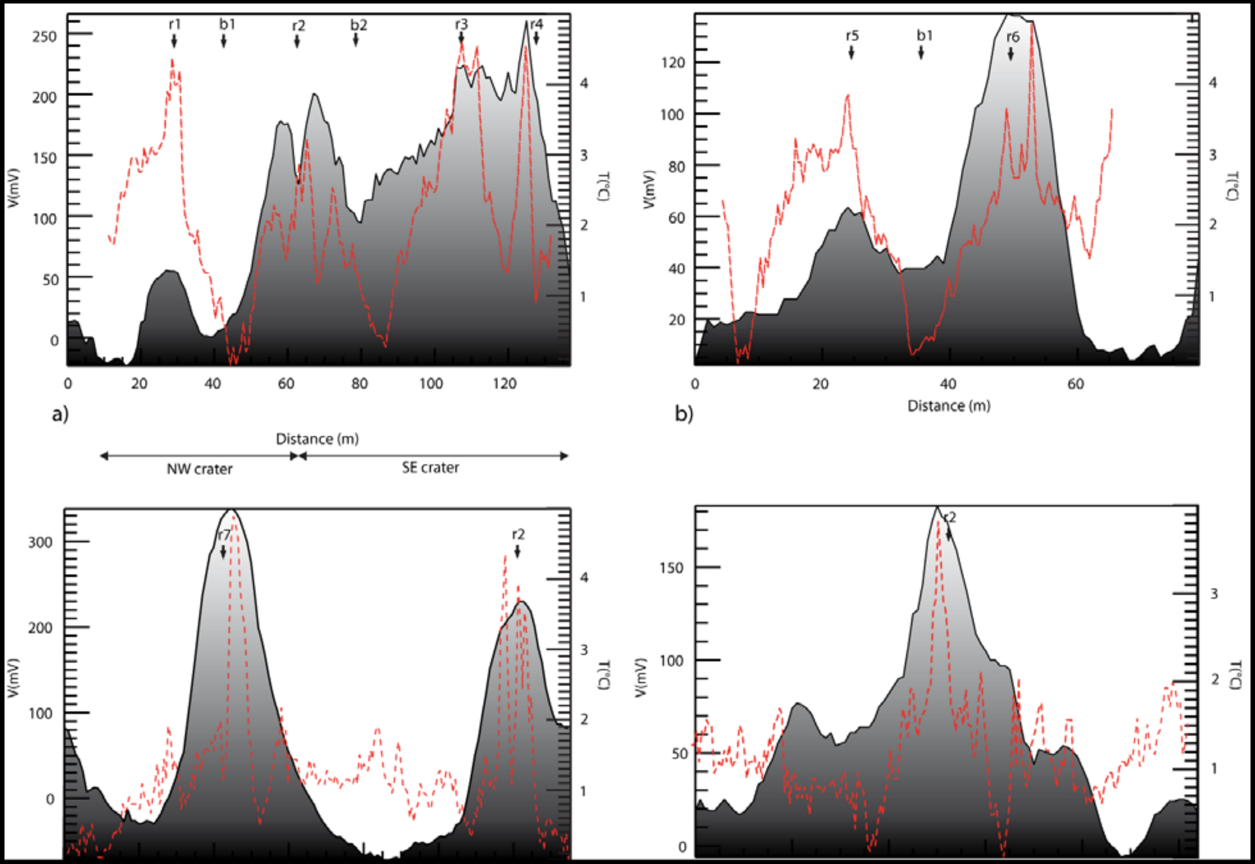

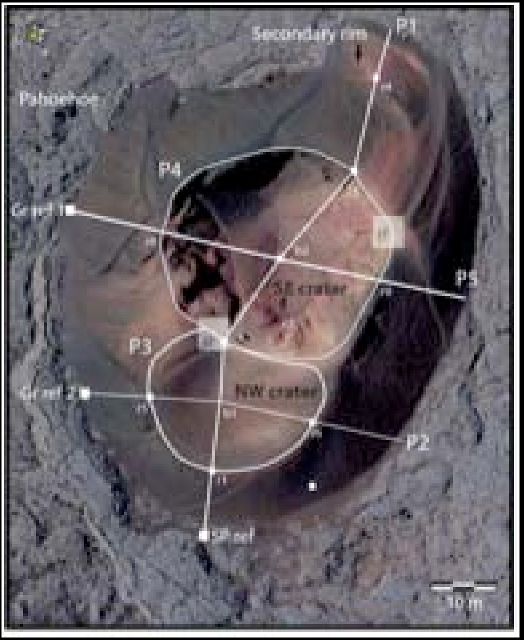

Picture of Formica Léo with the SP profiles (P1 to P5).

SP profiles (solid lines) and temperature profiles extrat from the thermal images (dotted lines).

Air convection within the craters can have an influence on the SP patterns.

Antoine et al., submitted 2009

Air convection at the scale of Piton de la Fournaise

Antoine et al., submitted 2009

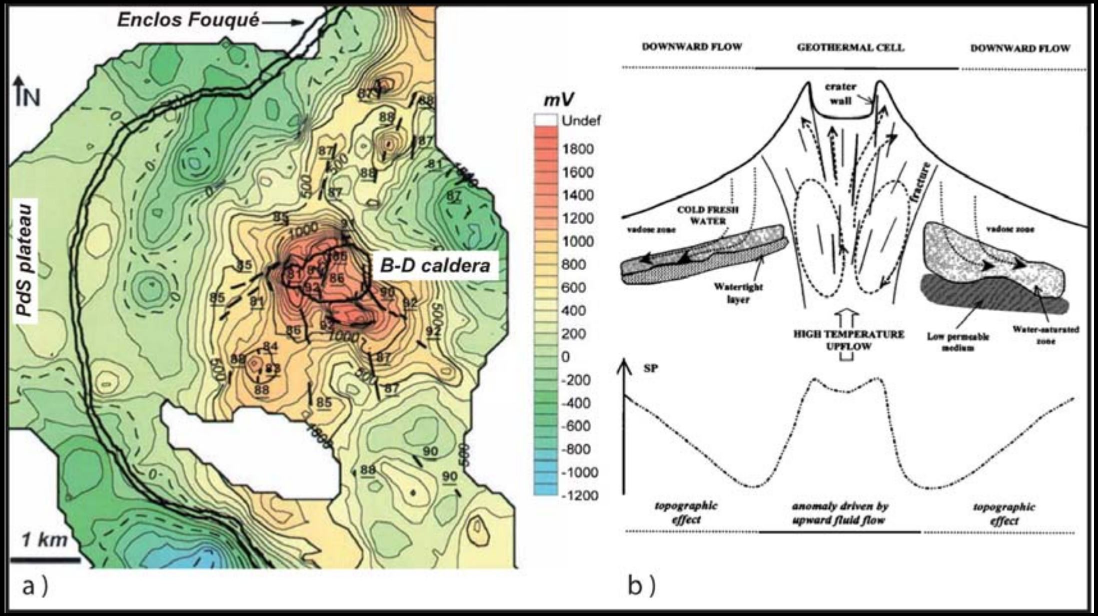

a) Piton de la Fournaise SP map. Two peaks, reaching 2V, are observed on the terminal cone.
b) Possible link with the meteoritic water infiltration.

a - b) Pluricentimetric and plurimetric fractures near the Bory-Dolomieu Caldera.
c – d) Fractures thermal images near the caldera (4 a.m)

Air convection at the scale of Piton de la Fournaise

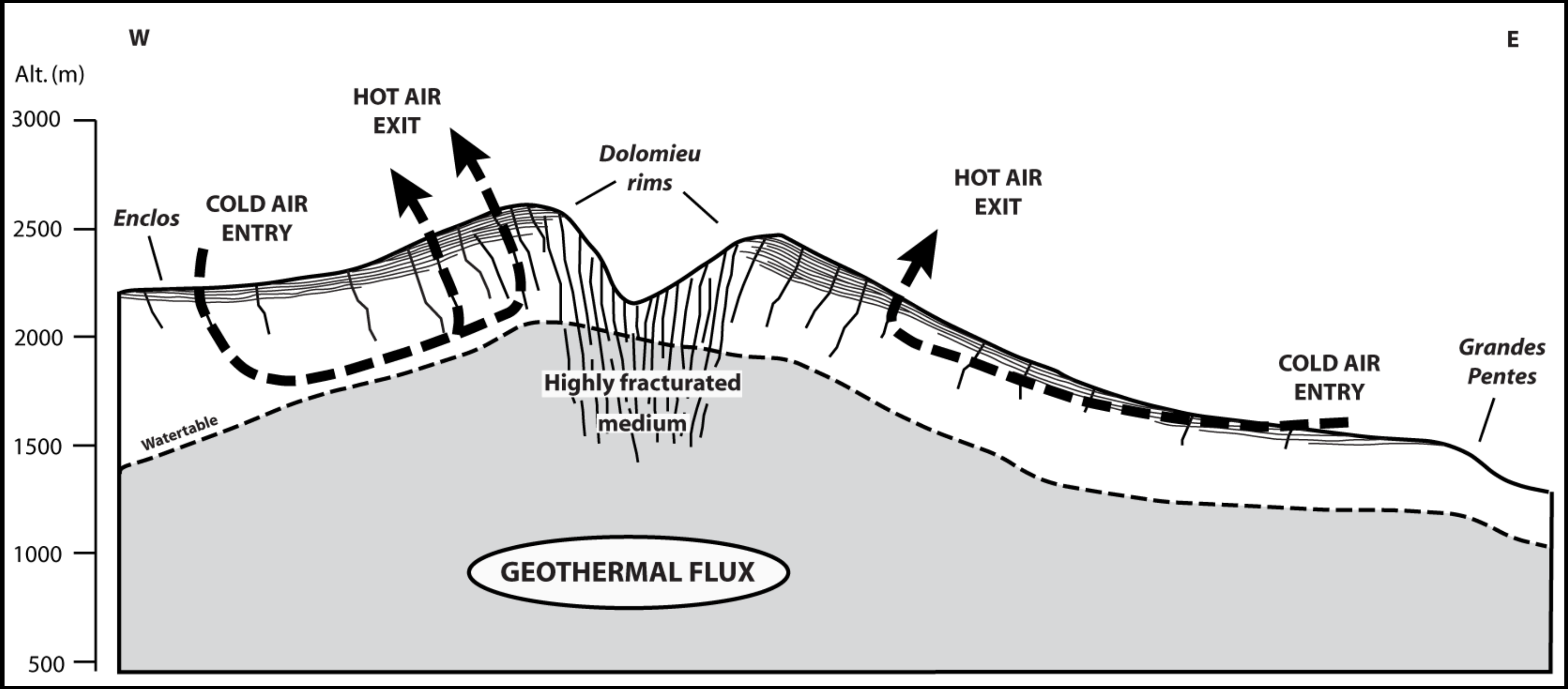

Like for Formica Léo, the existence of hot fractures at the Dolomieu edges can be explained by air convection. This air convection can have an impact in the SP pattern observed on this volcano.

Antoine et al., submitted 2009

Contents

Thermal data on Mars

- Radiance at the sensor,
- Surface temperature obtained by the black-body's law.

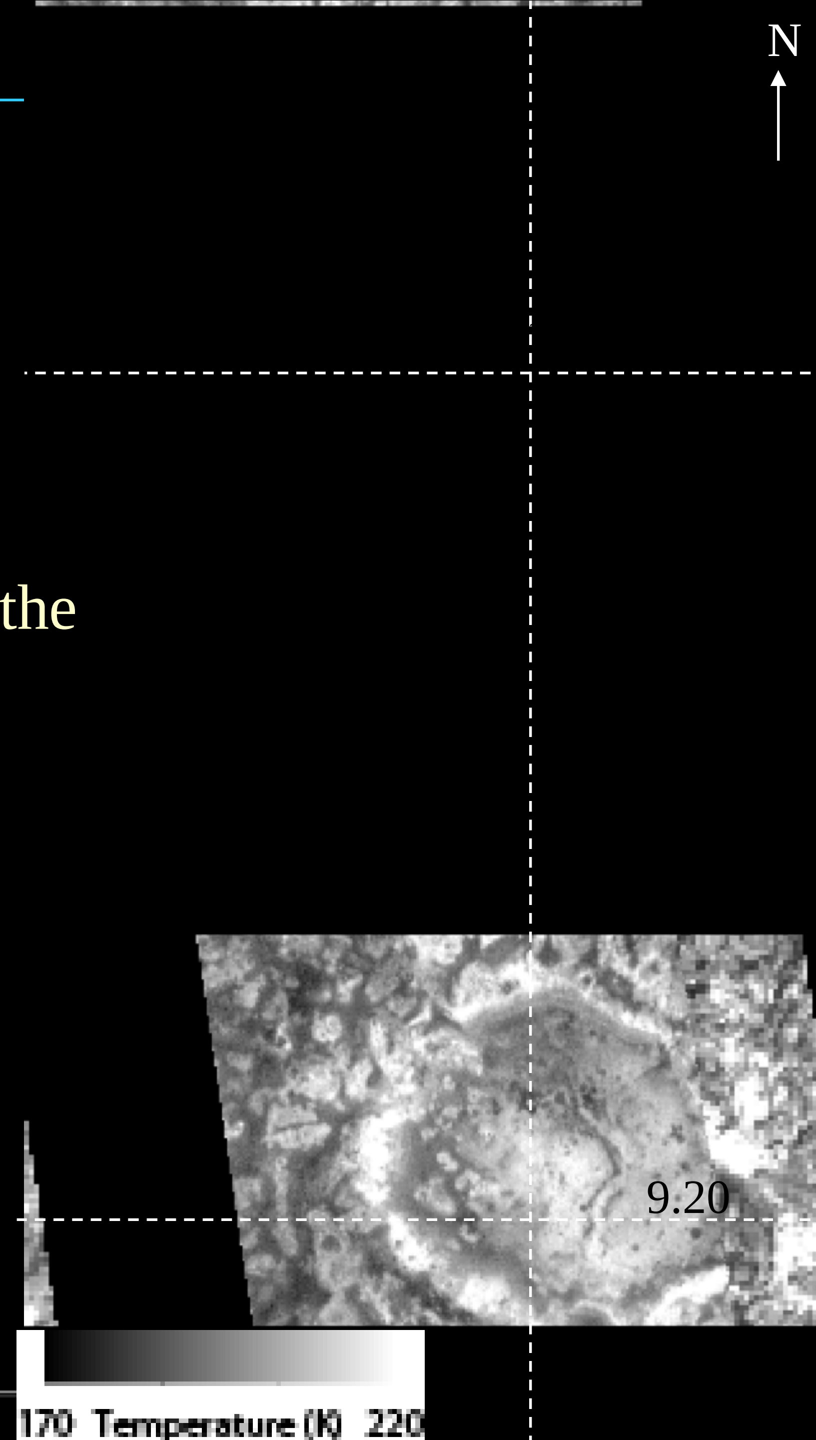

Surface Temperature : energy balance

(Mellon et al, 2000)

$$S/R^2 (1-A) \cos(i) + F_{IR} + L\, \partial m/\partial t + I \sqrt{(\pi/P * \partial T/ \partial z')} = \varepsilon\, \sigma T^4_S$$

- 1st term Insolation :

  S = solar flux, R = orbital radius, A = surface albedo, i = incidence angle.

- 2 nd term Thermal Radiation of atmosphere

- 3 rd term Saisonal CO_2 condensation:

  L = CO_2 latent heat of sublimation , m = mass of CO_2 frost.

- 4th term : Subsurface conduction:

  I = thermal inertia, P = diurnal period, T = temperature, z' = depth normalised

- 5 th term Radiations lost in space :

  ε = emissivity of the soil surface or CO_2, σ = Stefan-Boltzann constant, Ts = surface temperature.

Thermal inertia

- <u>Definition</u> :

$$\boxed{I = \sqrt{(k\rho c)}}$$

I = thermal inertia ($J/m^2/K/s^{1/2}$)

k = thermal conductivity ($W/K/m$)

ρ = density (kg/m^3)

c = thermal capacity ($J/kg/K$)

- <u>Practically</u> : It is the ability of the sub-surface to conduct and store heat energy away from the surface during day and to return that energy to the surface during the night.

Why temperature is varying?

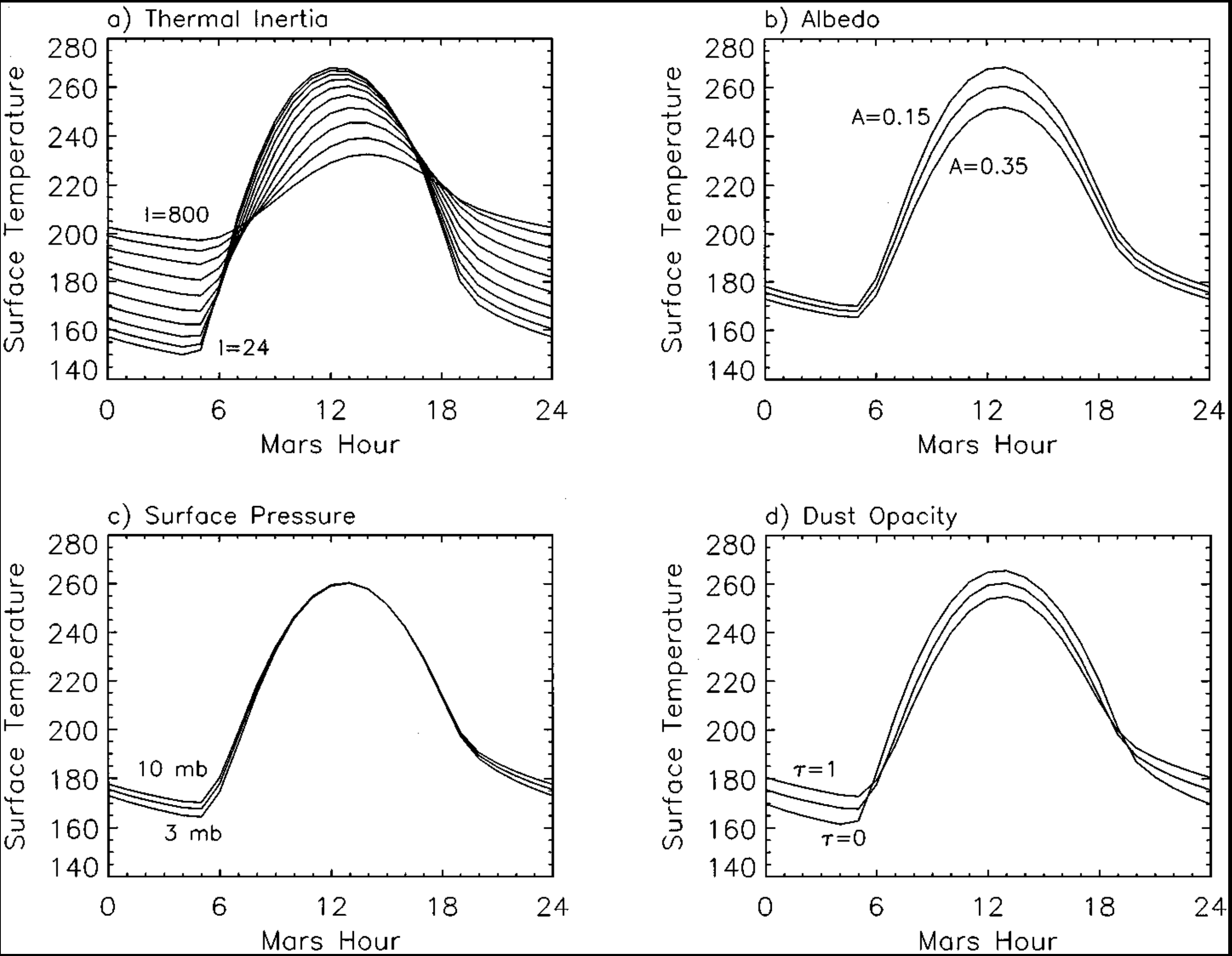

Influence of the thermal inertia, the albedo, the surface pressure and the dust opacity on the variation of diurnal surface temperature (Mellon et al, 2000)

Standard uses of thermal data

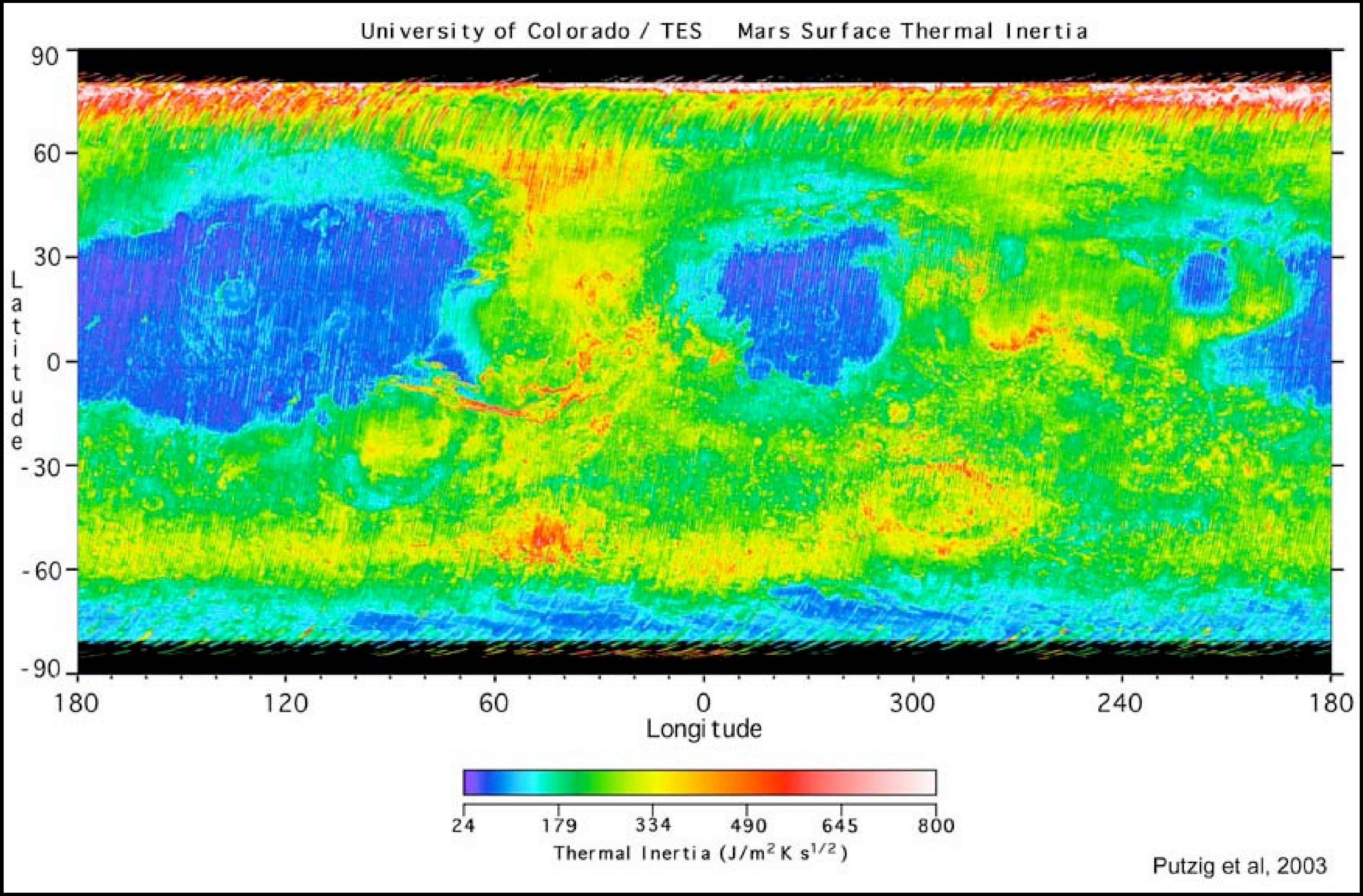

Martian surface temperature → Interpretation

Standard uses of thermal data

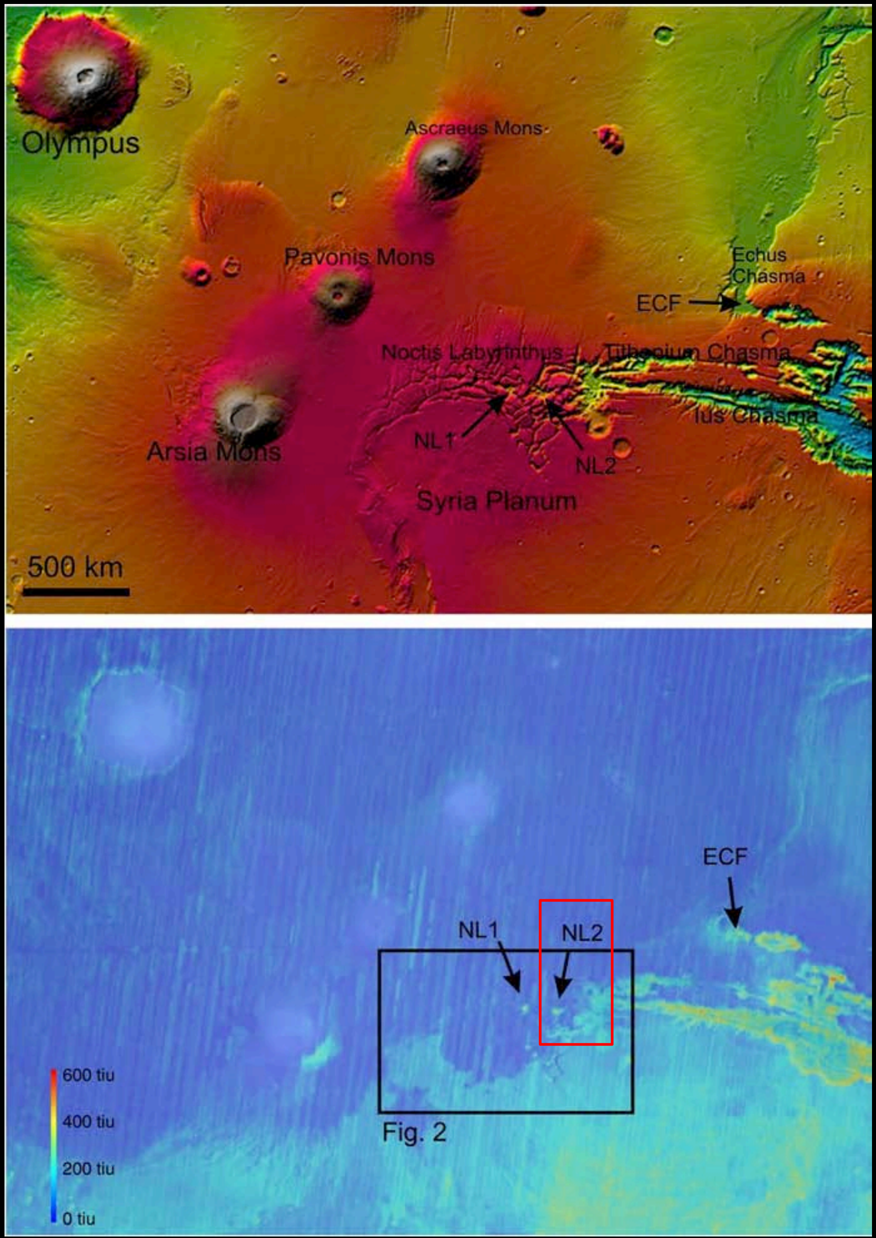

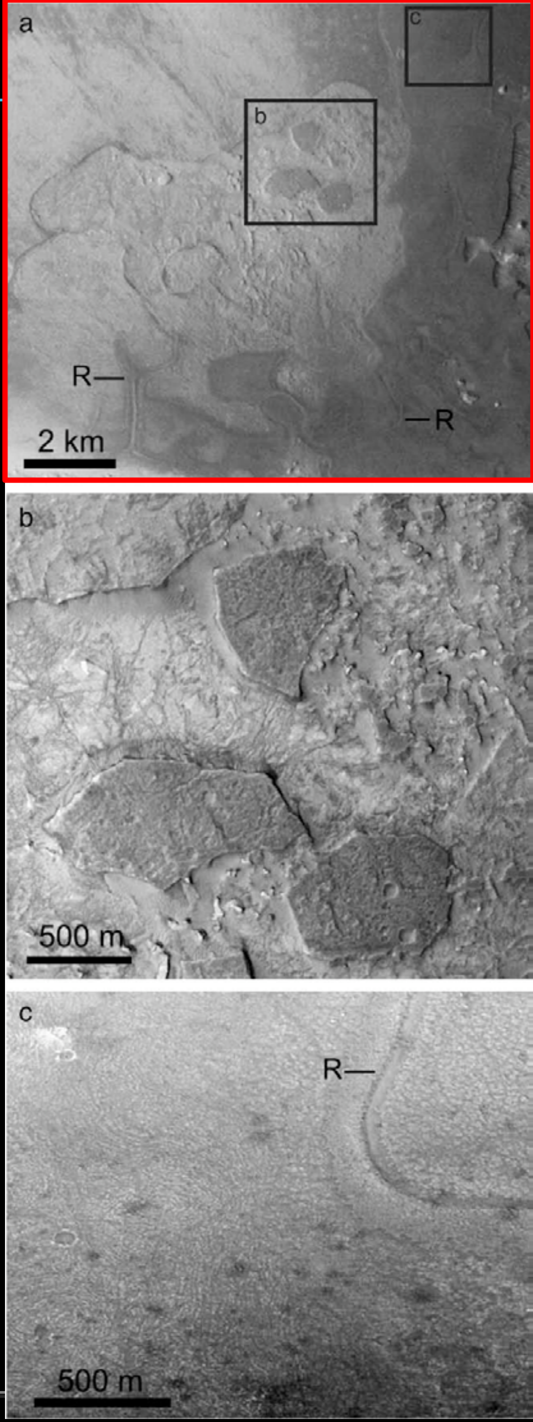

Mangold et al., EPSL 2009

Martian surface temperature → Interpretation

Contents

Cerberus Fossae

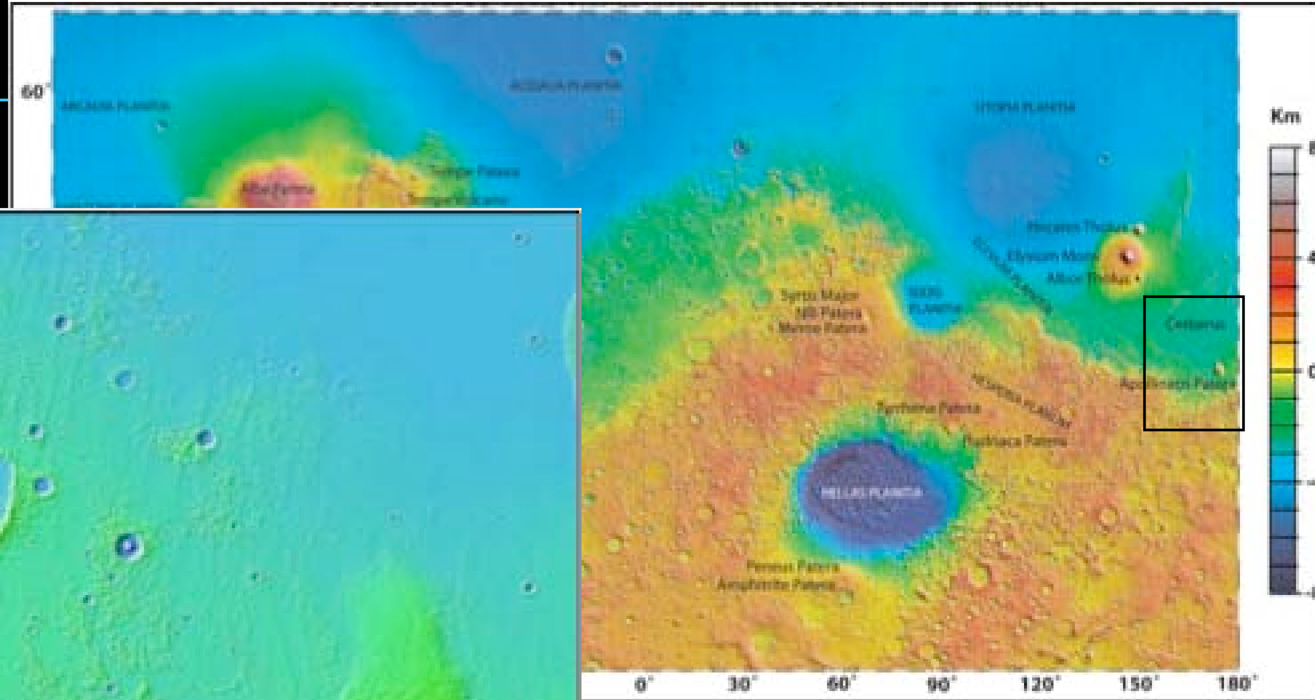

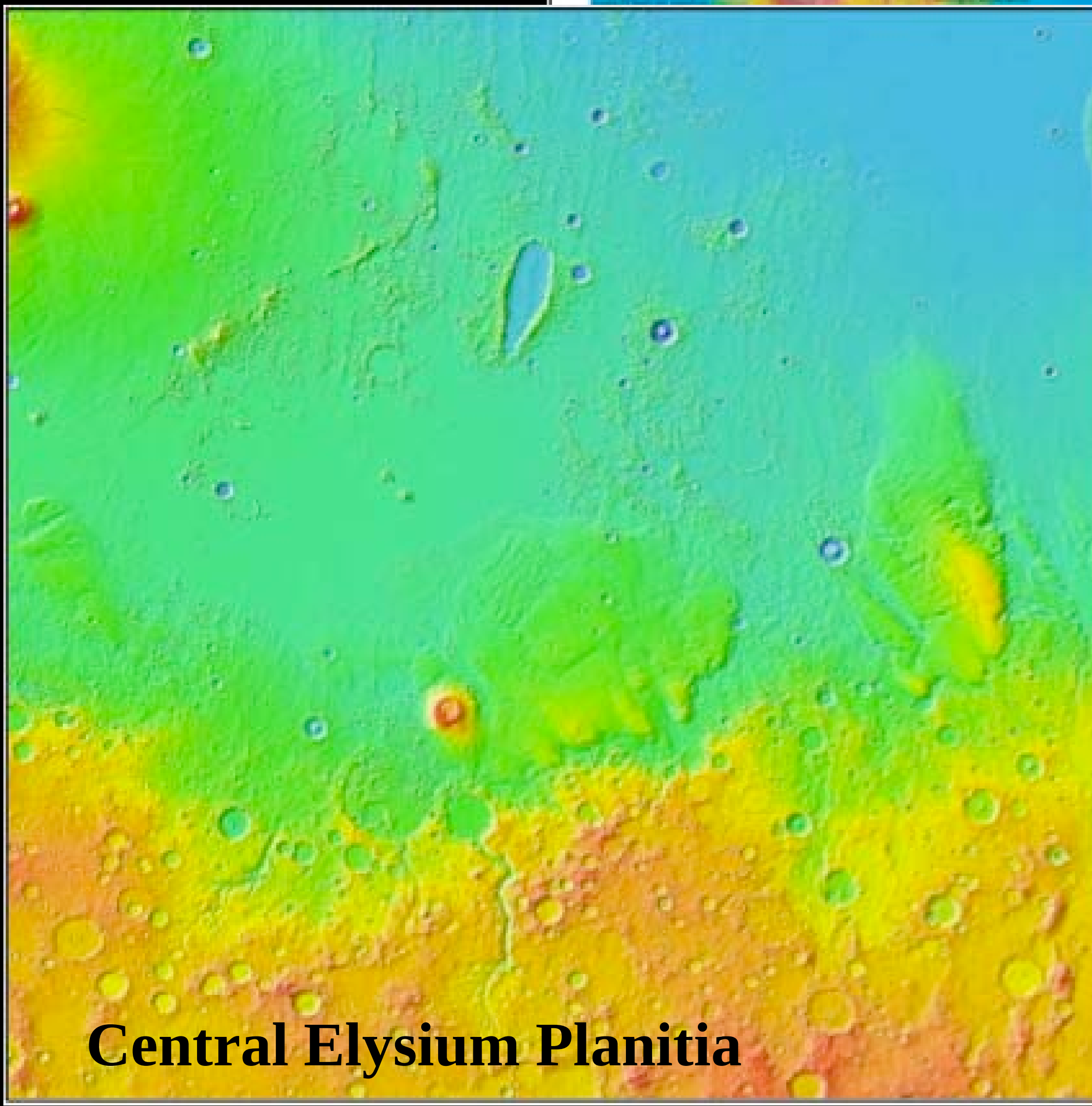

Context map : Location of Central Elysium Planitia.

Cerberus Fossae

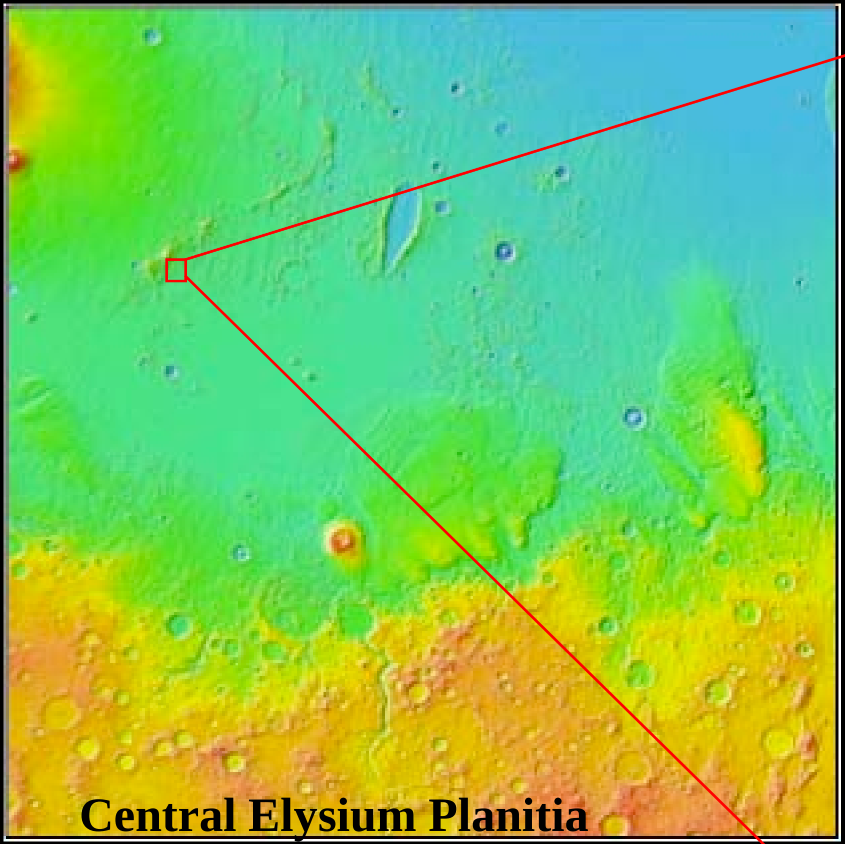

- Young volcanic plain,
- Fracture width: 2 km,
- Fracture depth: 600 m,
- Slope ≈ 30° .

Infrared image

- Two superposed thermal images in brightness temperature,
- Area warmer ≈ 220 K,
- Fracture center cold ≈ 190 K.

Relation between lithology and observed thermal behaviour?

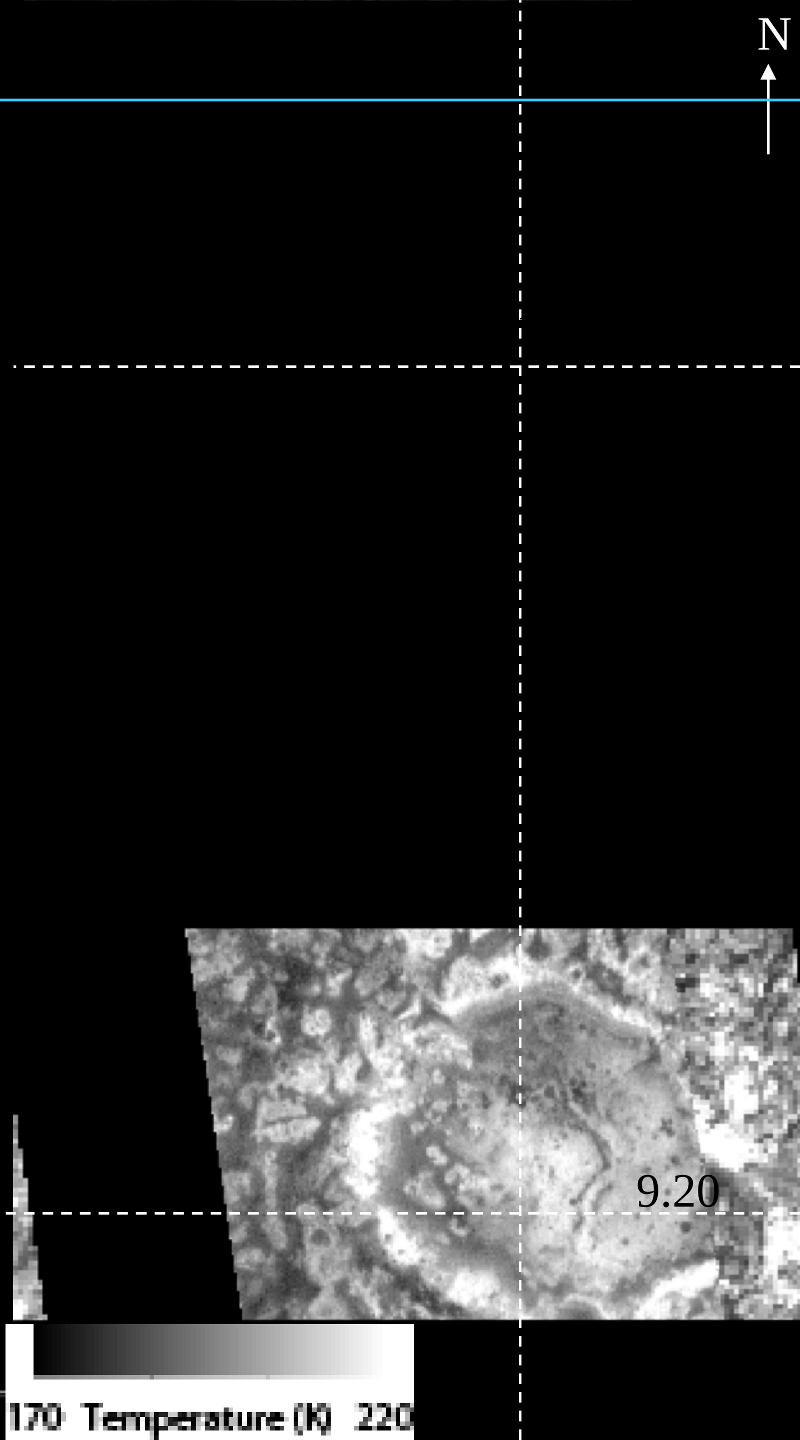

Antoine, Lopez et al., submitted 2009

Lithology _ Bedrocks

Antoine, Lopez et al., submitted 2009

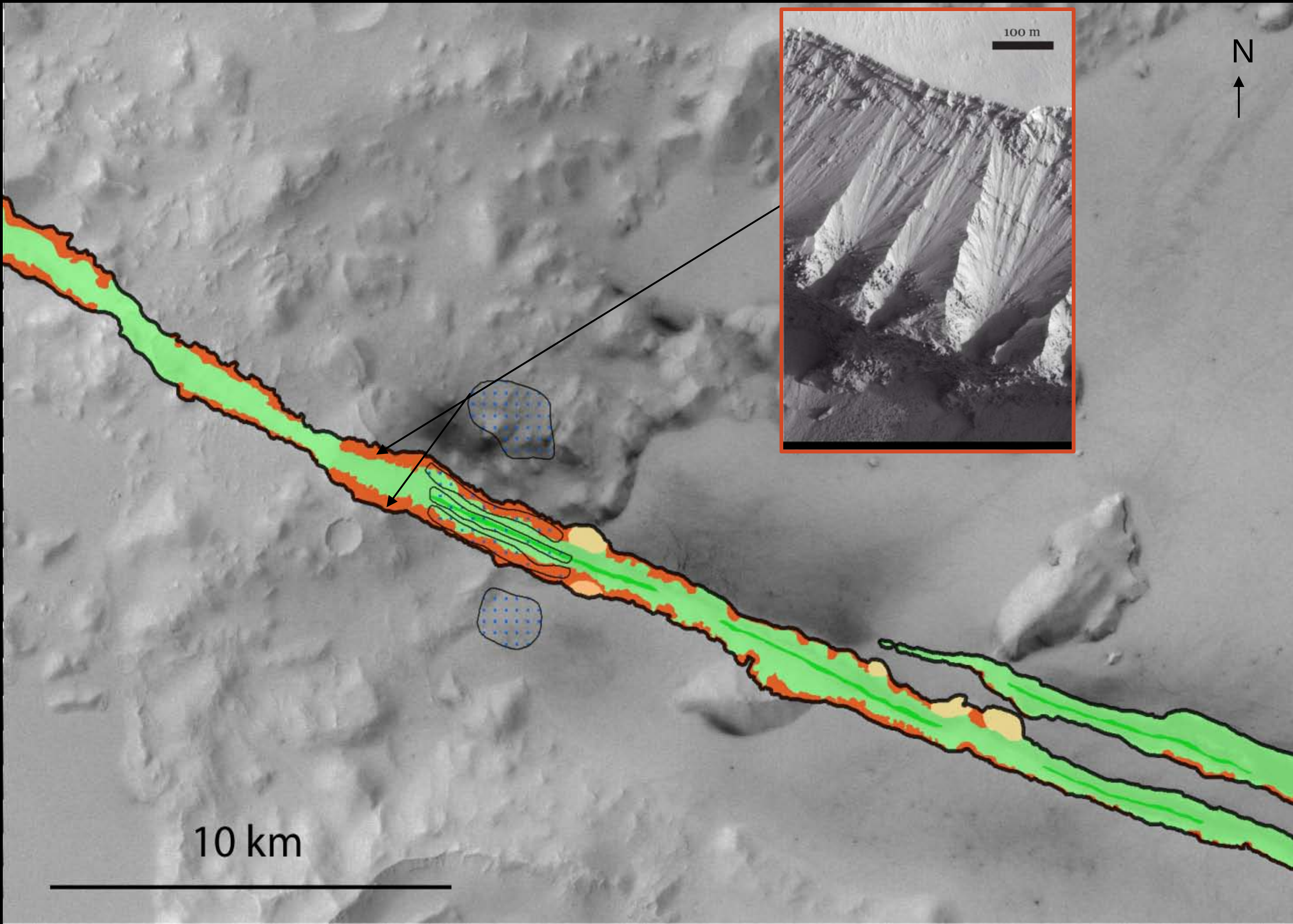

Lithology _ Landslides scars

Antoine, Lopez et al., submitted 2009

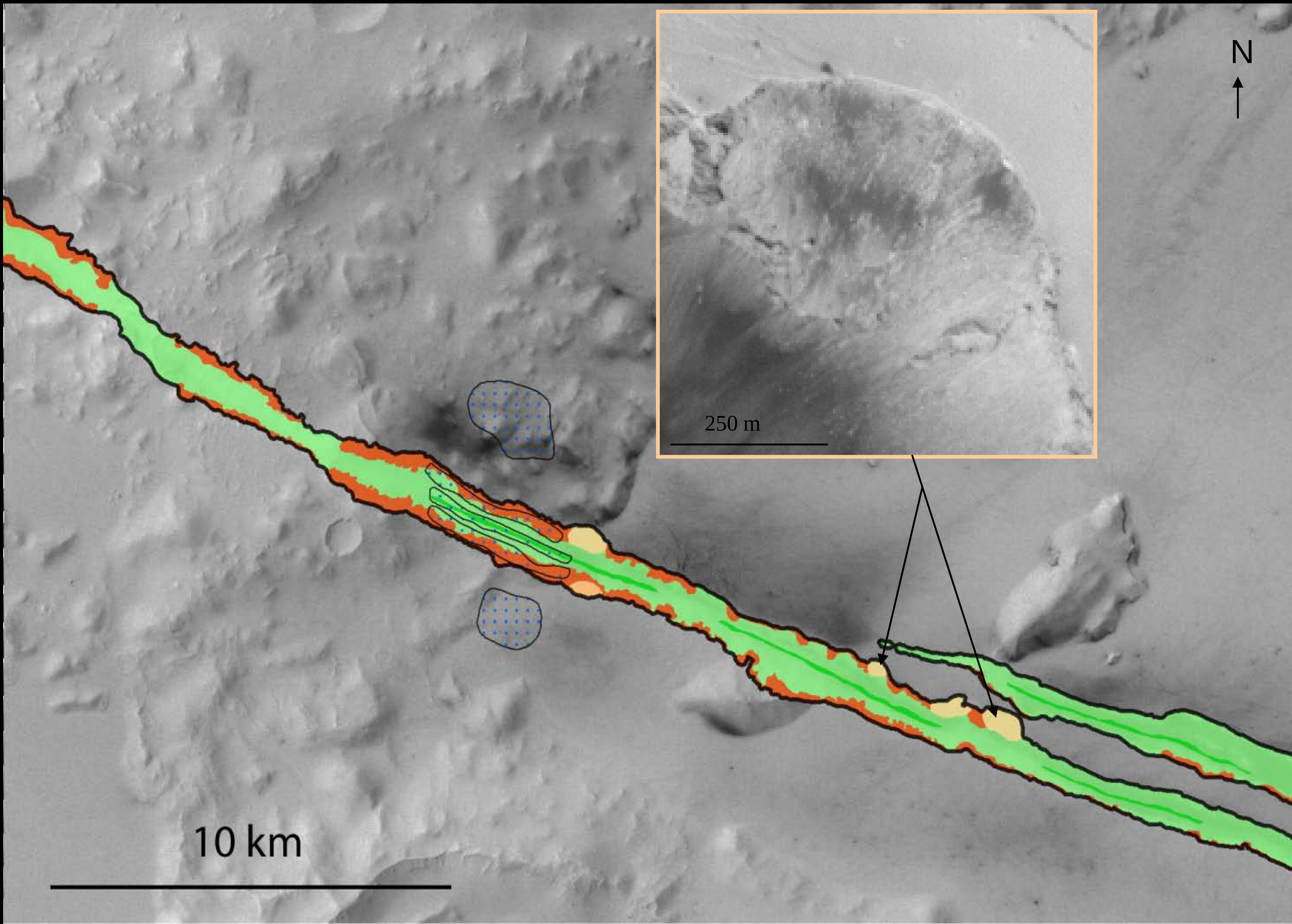

Lithology _ Debris Apron

Antoine, Lopez et al., submitted 2009

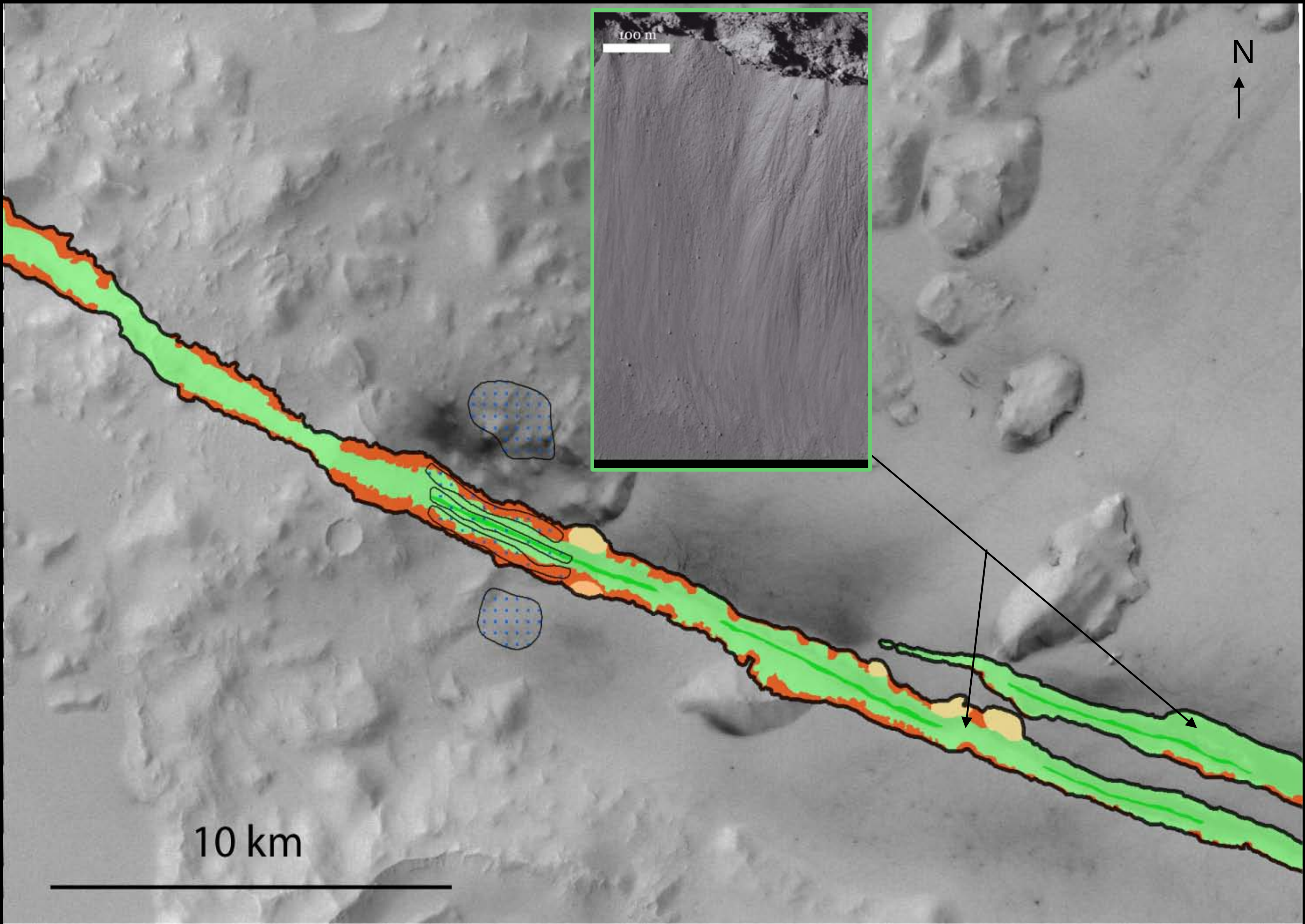

Lithology _ Dunes

Antoine, Lopez et al., submitted 2009

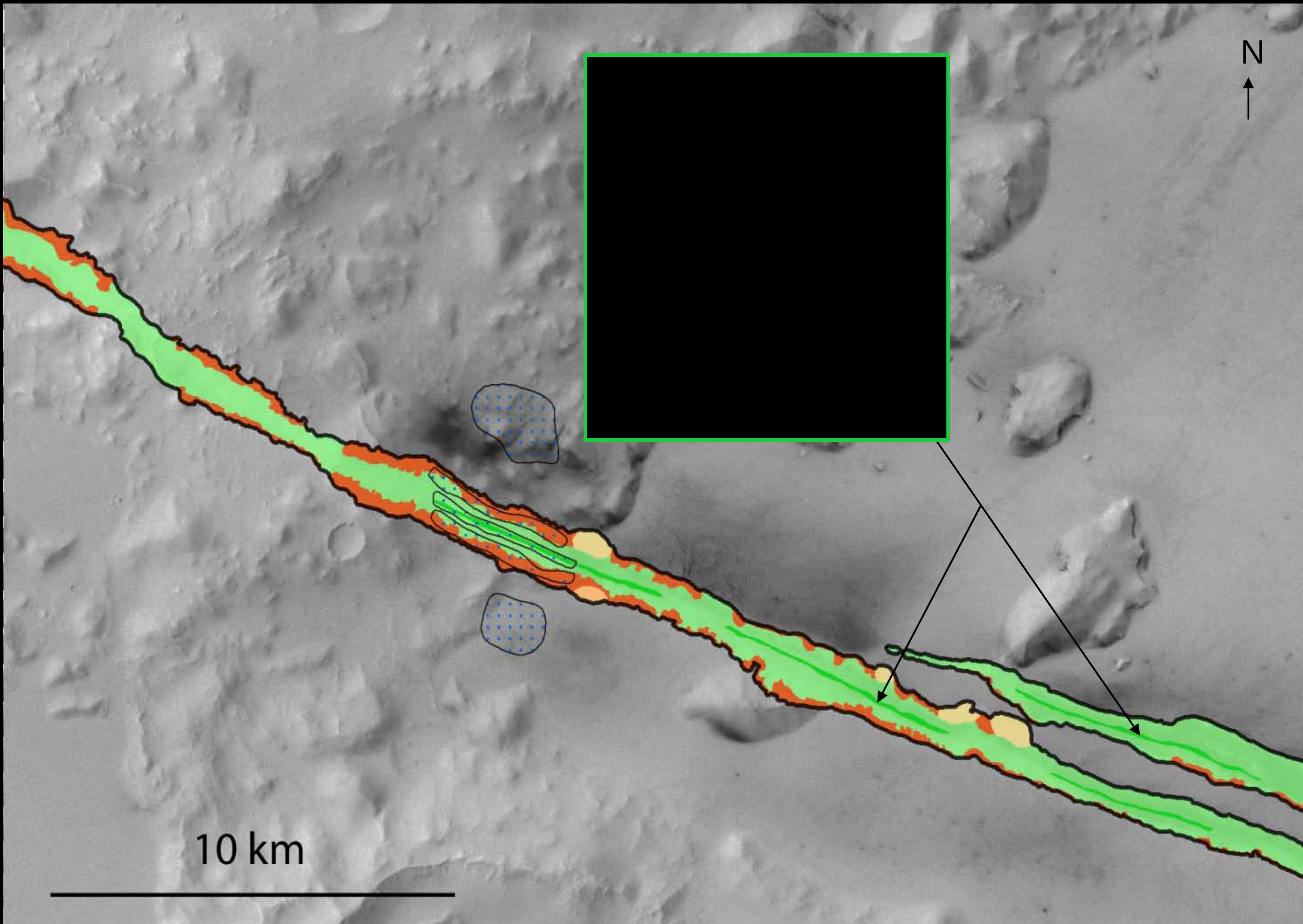

Mosaic of thermal images

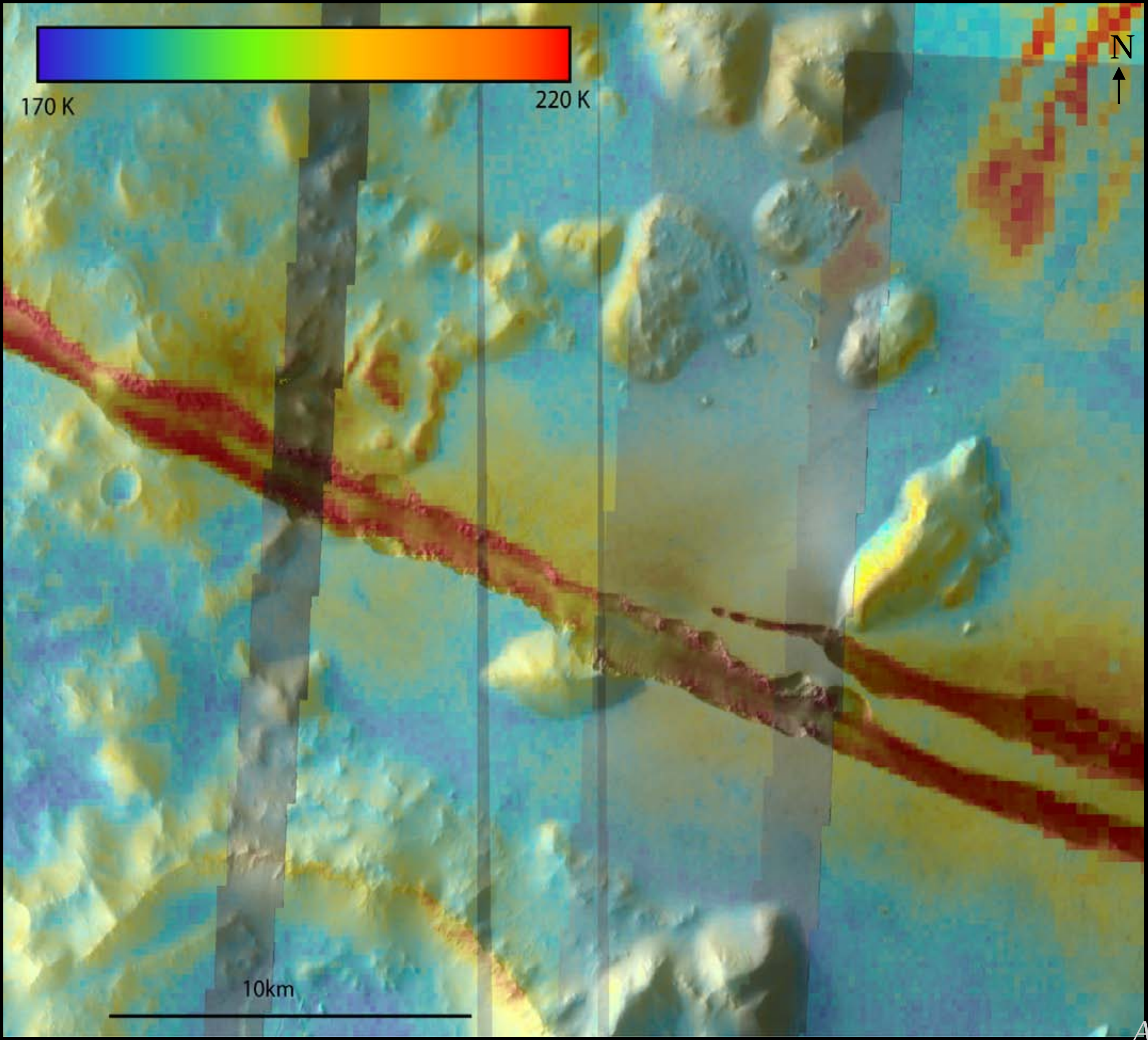

- THEMIS visible image under infrared nightime image

Antoine, Lopez et al., submitted 2009

Comparison between temperature and topographic profile

Thermal image of Cerberus Fossae. Temperature and topographic profiles across the fracture with dunes in the bottom.

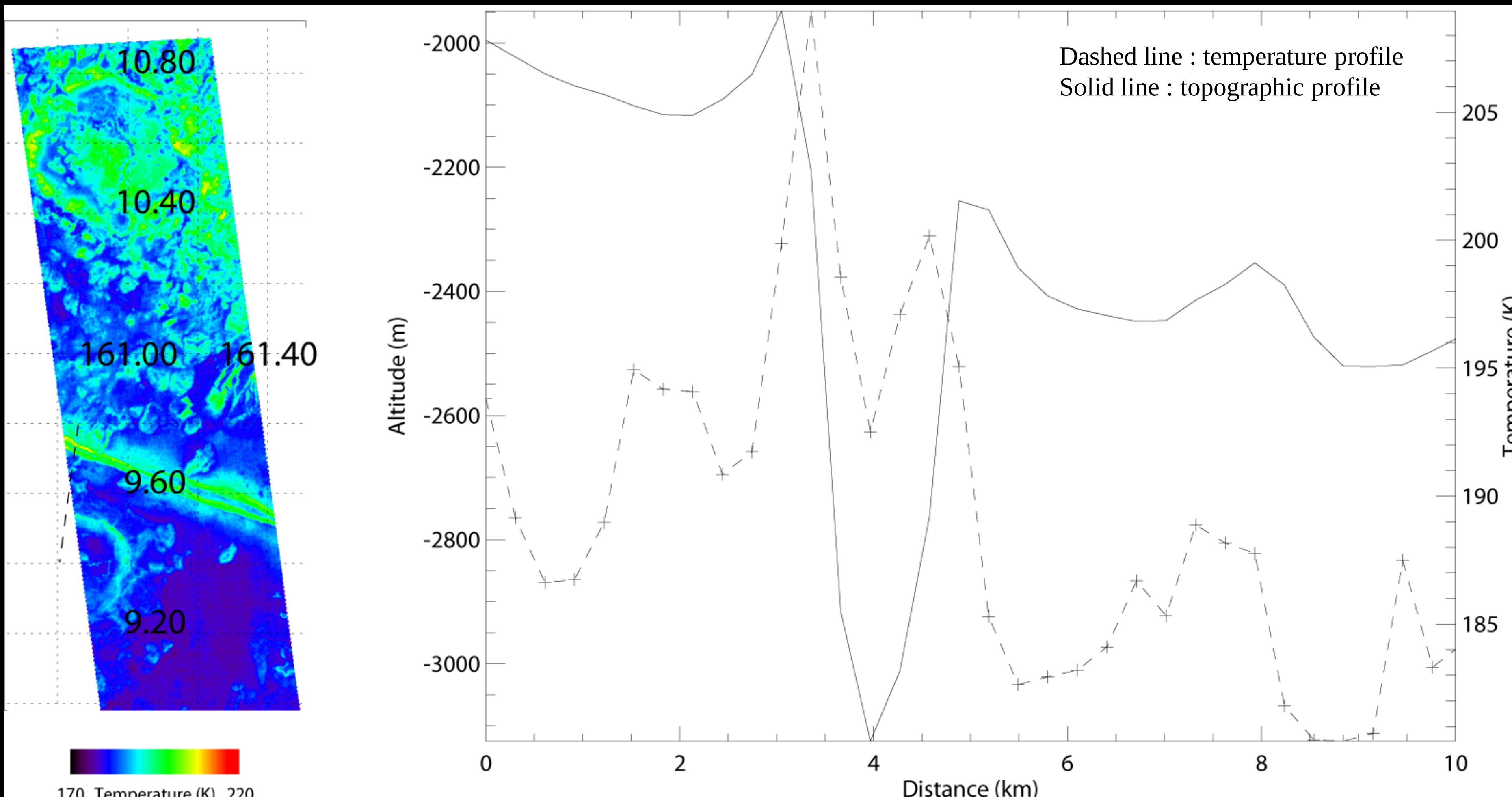

Antoine, Lopez et al., submitted 2009

Comparison between temperature and topographic profile

Thermal image of Cerberus Fossae. Temperature and topographic profiles across the fracture without dunes in the bottom.

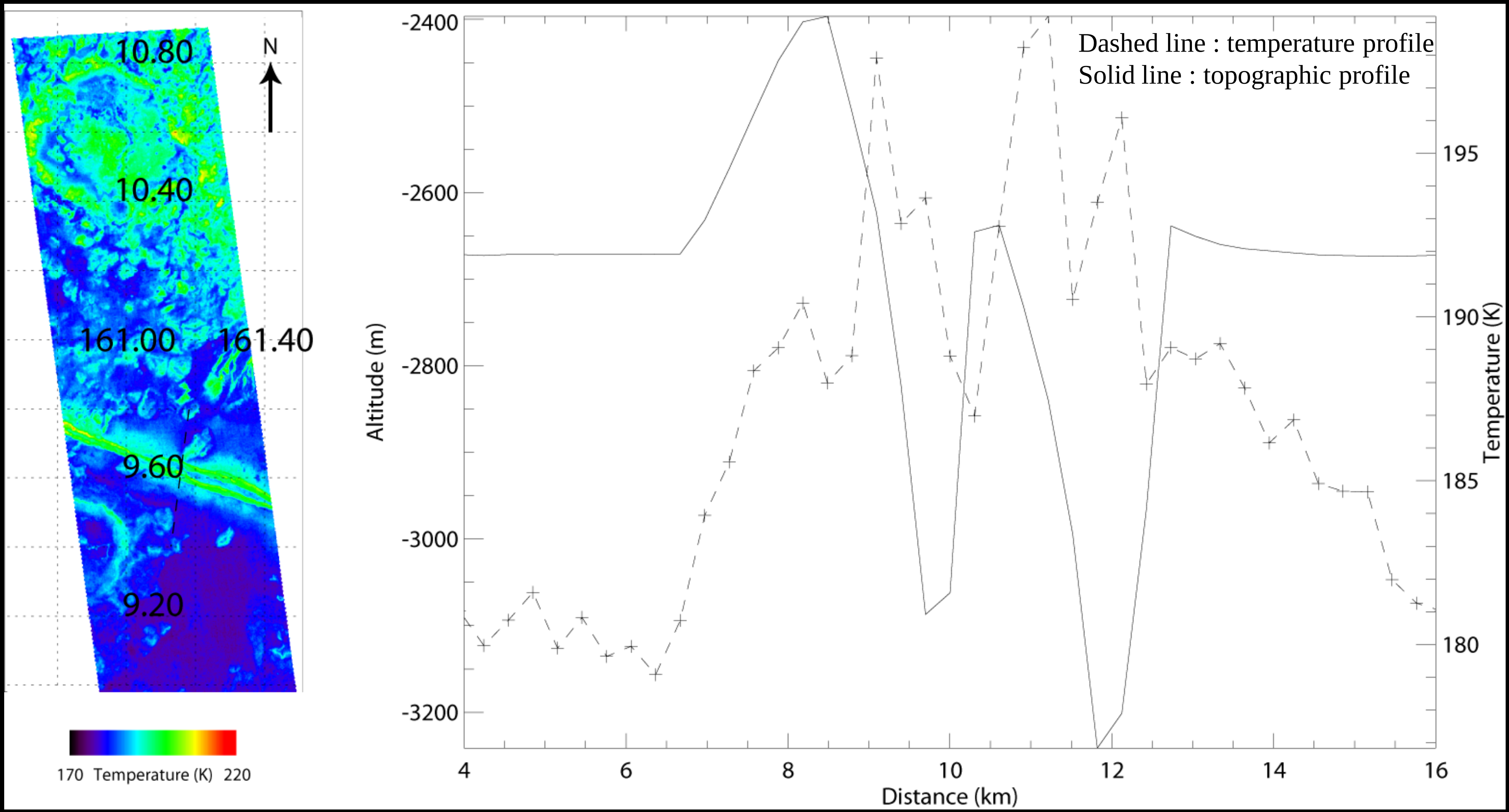

There are no influence of the lithology on the temperature variation.

Antoine, Lopez et al., submitted 2009

Numerical model of air convection

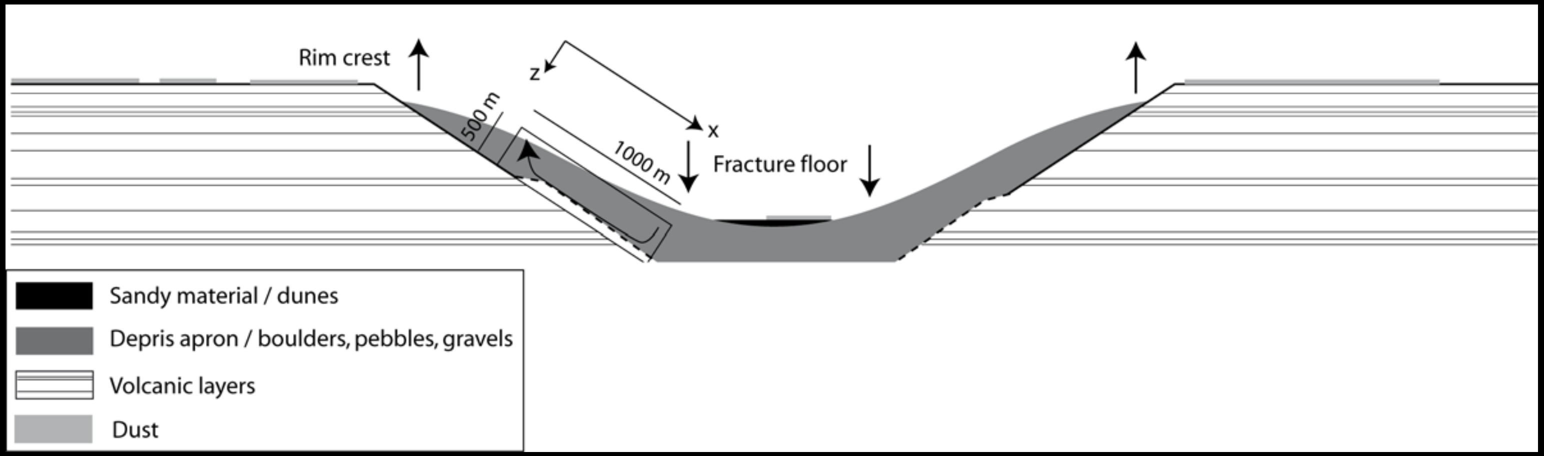

Representation of the box used for the air convection model.

Equations of the model:

$$\boxed{Ra = \rho_a \, g \, \alpha \, \Delta T \, H \, K / \mu \, \kappa}$$

$$\boxed{Ra_{eq} = \gamma \, Ra}$$

Notation and values used for the model

Height of the box	H	500 m
Length of the box	L	1000 m
Slope of the box		30°
Heat capacity of the air	C_a	850 J kg^{-1} K^{-1}
Heat capacity of the rocks	C_p	6.37 × 10^{-4} J kg^{-1} K^{-1}
Density of the porous debris aprons	$(1-n)\ \rho$	2000 kg/m^3
Air density	ρ_a	1.5 × 10^{-2} kg m^{-3}
Air thermal expansion	α	4.5 × 10^{-3} K^{-1}
Air Viscosity	μ	1.2 × 10^{-5} Pa.s
Air-soil volumic heat capacity ratio	γ	6.4 10^{-6}
Permeability of the soil	K	5 × 10^{-6} - 10^{-4} m^2
Thermal conductivity of the soil	k	0.4 W/m/K
Porosity of the soil	n	0.4
Top to bottom temperature contrast	ΔT	25 K
Average temperature of the atmosphere at the surface	T_0	180 K
Amplitude of diurnal temperature variations	A	40 K
Darcy velocity scale		6.3 × 10^{-5} m s^{-1}
Geothermal heat flux(for k = 2.5)		20 mW/m^2
Equivalent Rayleigh number	Ra_{eq}	41 - 830

Antoine, Lopez et al., submitted 2009

Model results

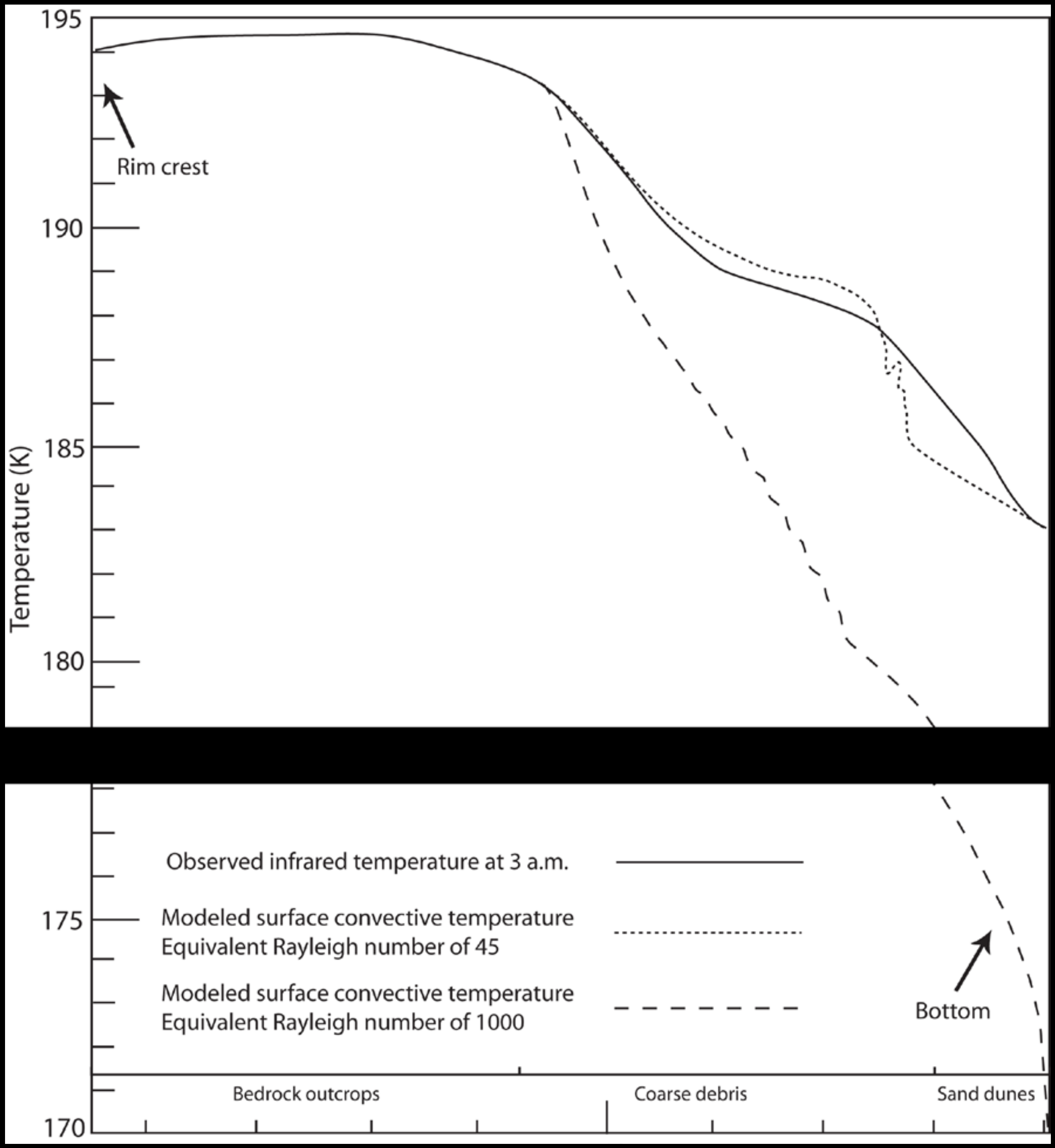

Plot of the observed infrared temperature (solid line), the surface convective temperature for a $Ra_{eq} = 45$ (dotted line) and the surface convective temperature for a $Ra_{eq} = 1000$ (dashed line)

The rim crest to floor temperature drop can be explained by a CO_2 convection for a $Ra_{eq} = 45$.

Antoine, Lopez et al., submitted 2009

Preliminary conclusions

- Lithology, topography and surface albedo do not explain the thermal pattern,
- CO_2 convection does explain the observed thermal behaviour :

  - convection permits the transport of heat through the debris apron,

  - for $Ra_{eq} = 45$, geothermal flux = 20 mW/m^2, the convective temperatures fit the observed temperatures.

- Presence of aerothermal systems on martian permeable soils.
- Others volcanic area might be possible candidates for this convection like the Tharsis region.

Contents

Arsia Mons and pits location

Lopez et al., in preparation, 2009

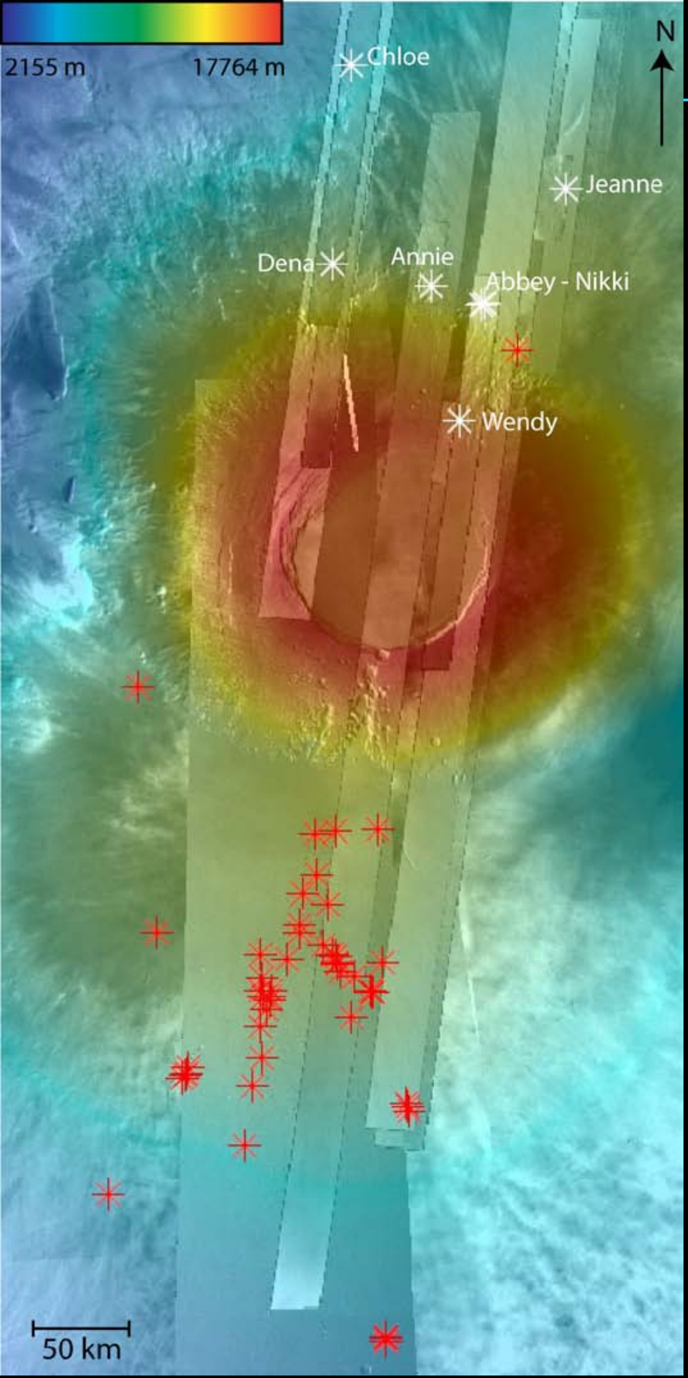

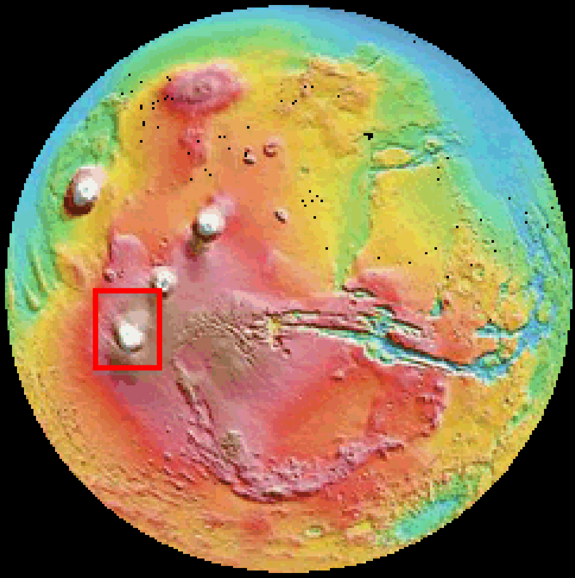

Context map : Location of Arsia Mons

Geographical Information System (GIS) with MOLA, HRSC and THEMIS visibles images. White cross are pits previously discovered (Cushing et al., 2007) and red cross are pits discovered during this study.

Pits presentation

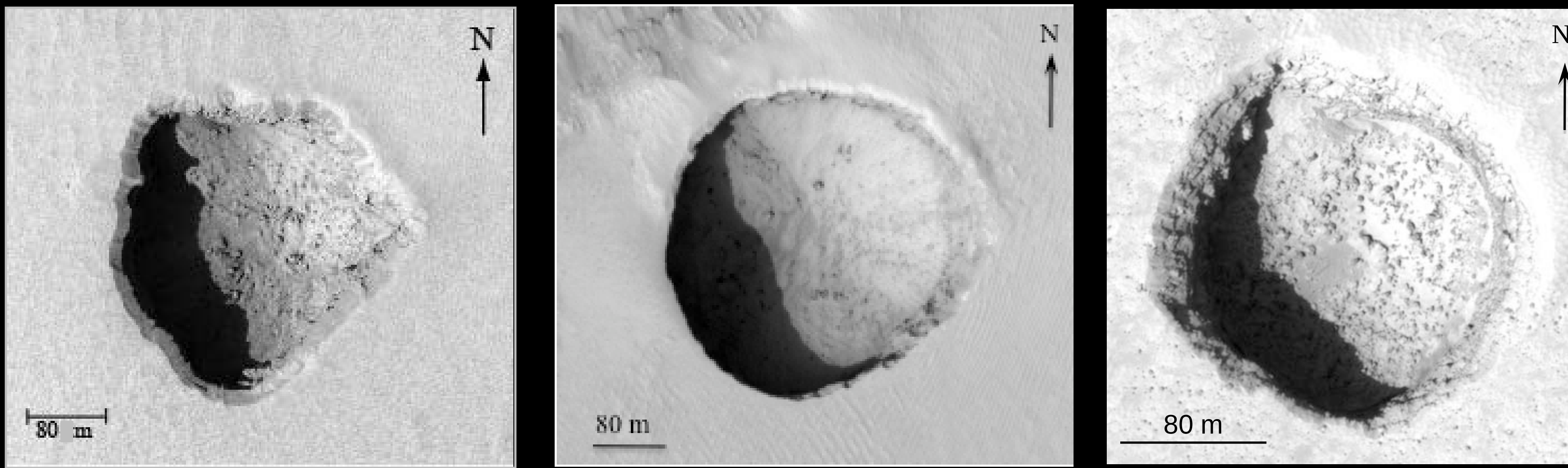

Three pits images extracts from HiRISE.

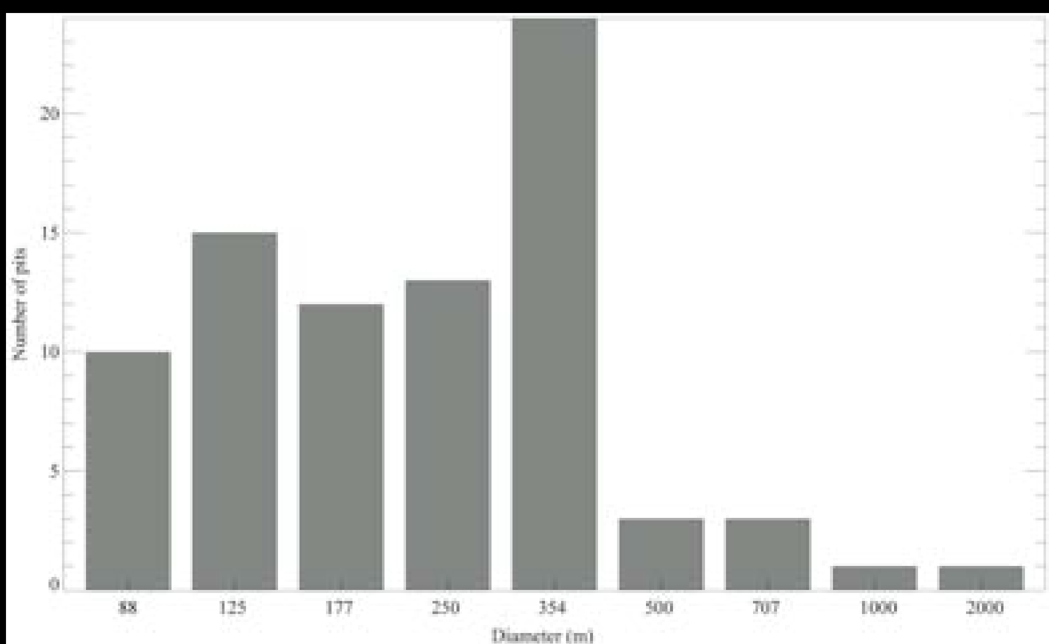

Bar charts of the pits size distribution using √2D interval of pits diameters.

Lopez et al., in preparation, 2009

Pits presentation

Lopez et al., in preparation, 2009

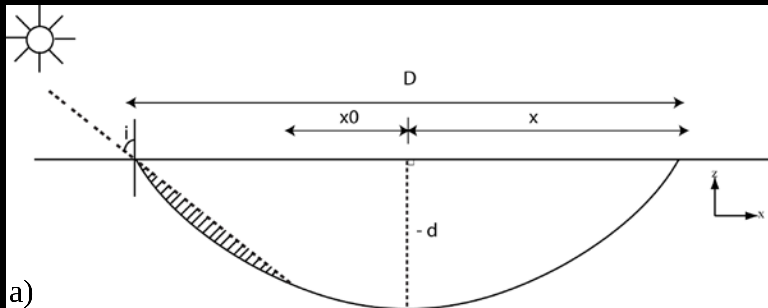

$$d = - D^2 \tan(90 - i) / 4(x_0 - D/2)$$

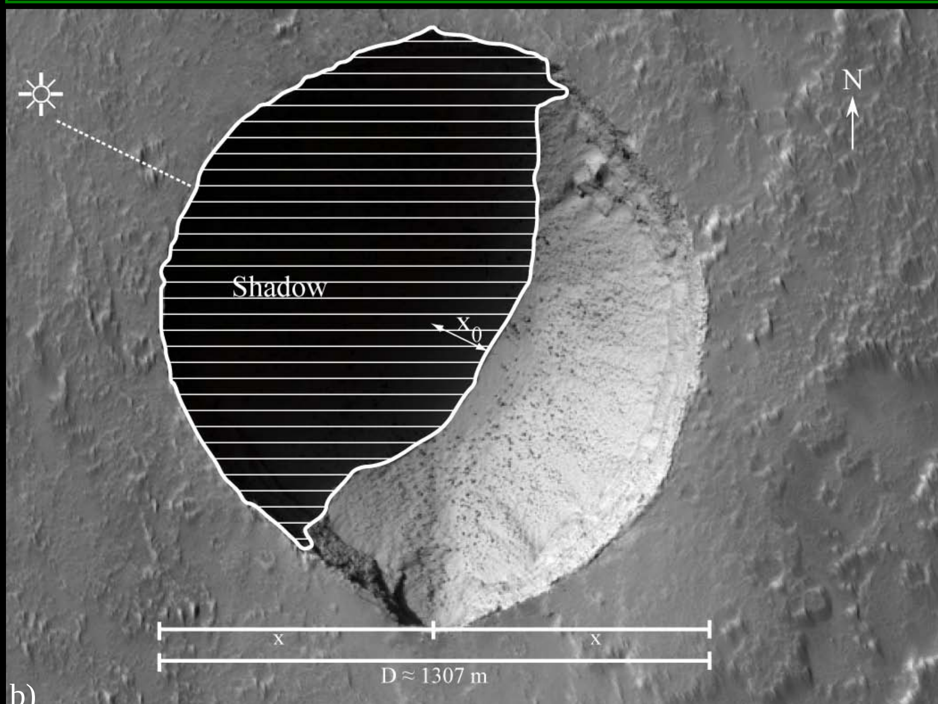

a) Schematic illustration of topographic model.

b) Application of the model in the biggest pit (i = 64°).

Incidence	Diameter(D)	X0	x0/D	Depths(d)	d/D	δd/d	
34.00	198.50	-25.00	-0.12	117.53	0.45	0.73	
38.00	287.04	-48.62	-0.16	137.21	0.44	0.63	
40.00	198.75	-33.13	-0.16	88.81	0.44	0.58	
41.00	170.30	45.11	0.26	208.31	0.43	0.58	
36.00	216.25	-12.63	-0.05	133.25	0.42	0.68	
37.00	152.500	-23.75	-0.15	77.15	0.42	0.65	
36.00	103.00	-15.25	-0.14	54.68	0.41	0.67	
34.40	116.50	6.07	0.05	94.96	0.40	0.74	
64.00	330.00	-33.50	-0.10	66.89	0.40	0.24	
64.00	985.00	122.50	0.12	319.73	0.39	0.24	
64.00	1307.30	167.85	0.12	428.95	0.38	0.24	
64.00	379.500	-32.75	-0.08	78.92	0.38	0.24	
59.00	333.50	20.75	0.06	114.43	0.37	0.30	
50.00	166.75	-7.38	-0.04	64.27	0.37	0.41	
33.92	265.00	-74.86	-0.28	125.90	0.36	0.63	
64.00	364.00	-30.50	-0.08	76.02	0.36	0.24	
33.92	652.00	-231.68	-0.35	283.38	0.35	0.69	
33.92	249.00	-87.82	-0.35	108.55	0.35	0.63	
33.92	261.00	-88.58	-0.33	115.59	0.34	0.63	
-0.38	115.79	0.34	0.63	33.92	276.00	-106.56	
-0.36	82.29	0.33	0.60	33.92	191.00	-69.30	
-0.32	190.29	0.33	0.68	33.38	412.50	-133.03	
-0.38	285.32	0.32	0.71	33.38	663.00	-253.05	
-0.18	55.59	0.32	0.53	33.38	101.00	-19.12	
-0.22	59.36	0.31	0.54	33.38	113.00	-25.12	
-0.12	130.13	0.31	0.26	60.19	571.50	-73.75	
-0.03	54.99	0.30	0.23	60.19	207.00	-8.10	
-0.09	69.27	0.30	0.24	60.19	287.50	-27.15	
0.22	57.47	0.29	0.47	60.19	109.25	24.88	
-0.06	43.23	0.29	0.22	60.19	170.50	-11.05	
-0.22	75.94	0.29	0.24	61.91	411.60	-91.84	
-0.41	147.41	0.28	0.68	32.81	346.00	-141.92	
-0.28	84.15	0.28	0.61	32.81	171.00	-49.24	
-0.27	81.34	0.27	0.61	32.81	163.17	-45.33	
-0.16	62.75	0.27	0.55	32.81	107.00	-17.24	
-0.39	155.23	0.27	0.68	32.81	360.00	-143.74	
0.10	46.01	0.26	0.38	62.23	136.50	14.95	
-0.35	172.35	0.26	0.67	33.44	388.50	-137.27	
-0.37	125.53	0.25	0.47	43.67	420.00	-158.00	
-0.35	44.84	0.25	0.40	43.67	147.00	-52.70	
0.93	40.51	115.00	25.22	0.21	119.88	0.25	
0.99	40.51	103.50	20.63	0.19	100.72	0.24	
0.40	47.00	299.00	-135.7	-0.45	73.07	0.24	
0.28	58.09	518.00	-29.76	-0.05	144.65	0.24	
0.26	58.09	244.90	-80.77	-0.32	45.94	0.23	
0.28	58.09	414.00	-87.17	-0.21	90.70	0.23	
0.35	58.09	333.50	41.65	0.12	138.40	0.23	
0.28	58.09	491.00	-31.89	-0.06	135.29	0.22	
0.25	61.04	483.00	-134.90	-0.27	85.74	0.22	
0.24	61.04	391.00	-99.56	-0.25	71.68	0.22	

Morphological values

Relation between pits and geomorphology

Legend

- Slide terrain
- Collapse unit
- Smooth unit
- Hummocky unit
- Aligned features
- Lava channels features
- Sinuous rilles
- Raised ridges

Lopez et al., in preparation, 2009

Morphological map made with HRSC images.

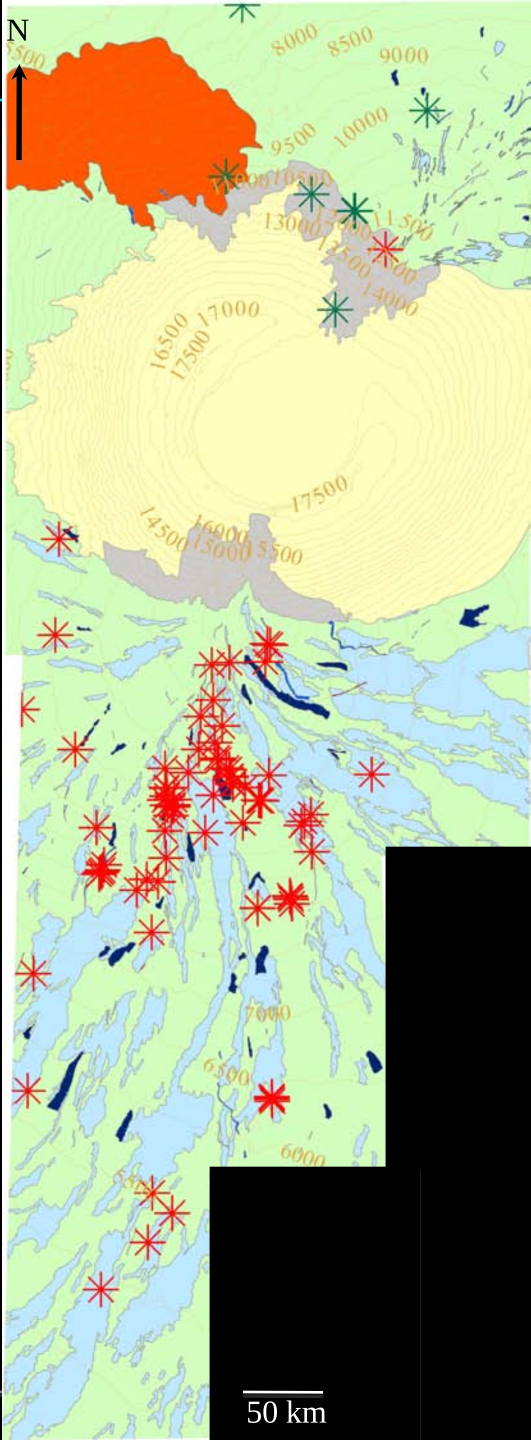

Relation between pits and geomorphology

Preferential direction NE-SW > Tharsis Montes rift zone (extension area, Mouginis-Mark and Christensen, 2005)

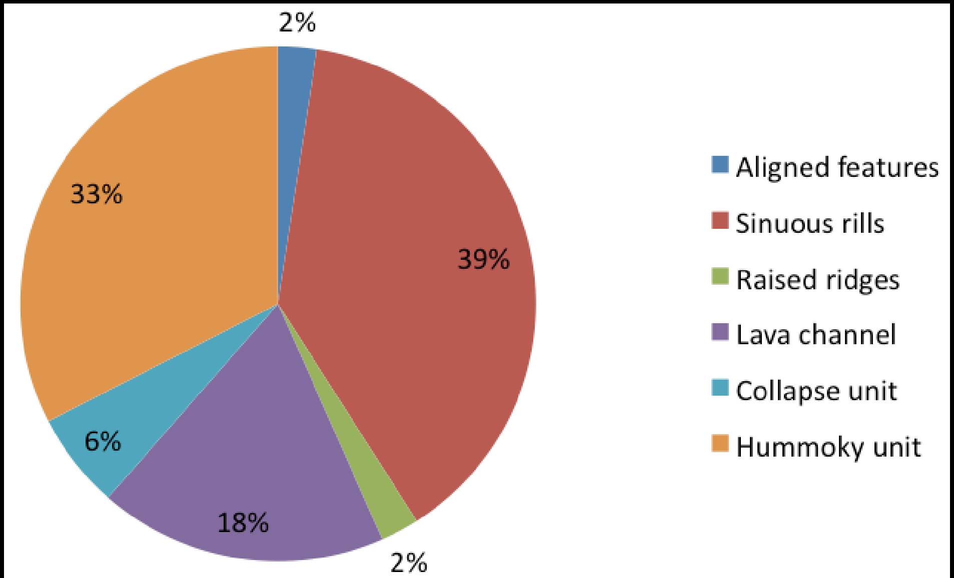

Pits repartition in taking account the morphology associated at each pits. Sinuous rilles have the most important numbers of pits.

Lopez et al., in preparation, 2009

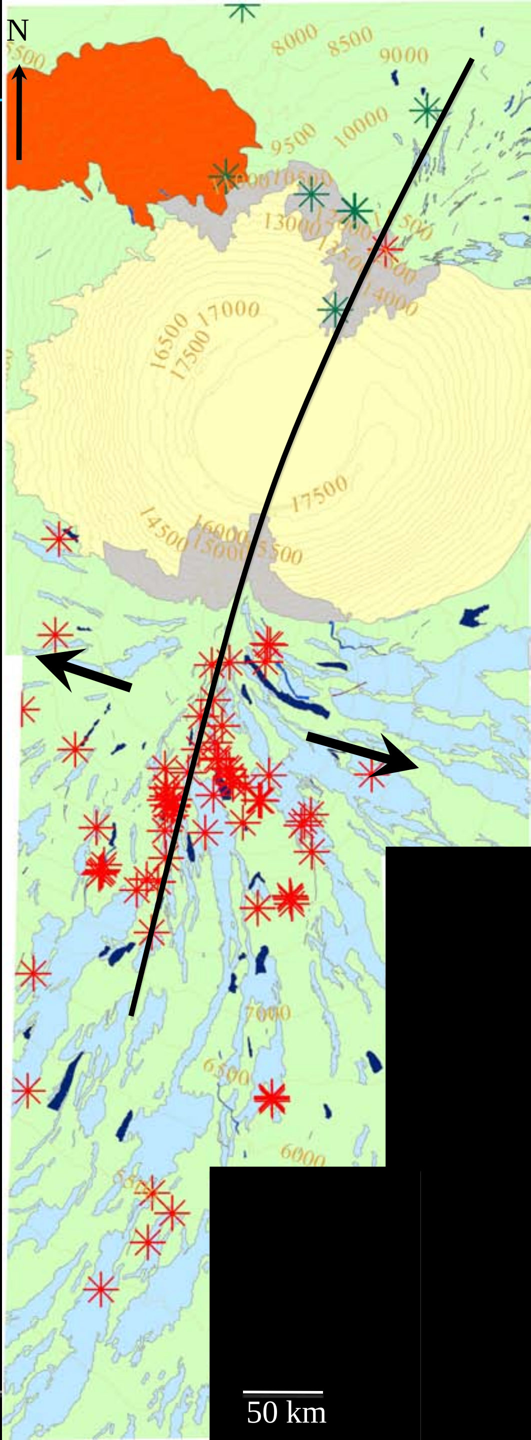

Thermal study of the pits

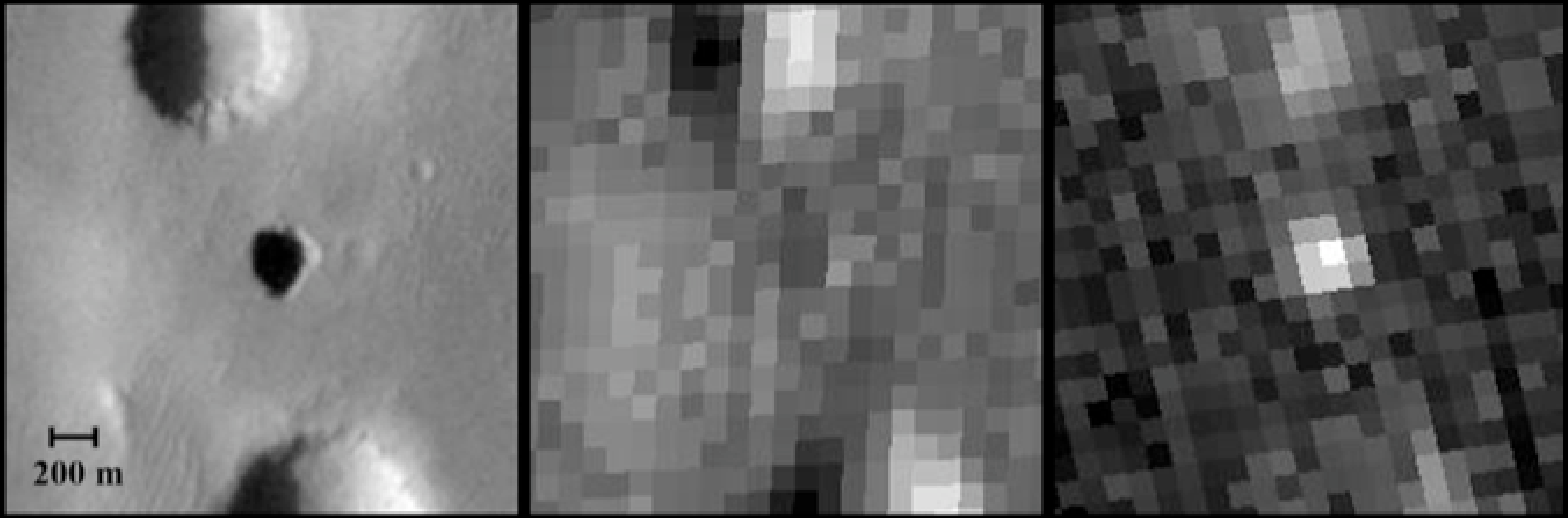

Extracts of THEMIS visible (a), infrared daytime (b) and infrared nightime (c) images (Cushing et al, 2007)

The study of the pits thermal signal is interesting because of their temperature. They are, in average, 10K warmer than the surroundings. Is this observation is compatible with a CO_2 convection?

Thermal behaviour of Annie

Plot of the thermal pattern at different acquisition date. Right corner extract from a THEMIS visible image.

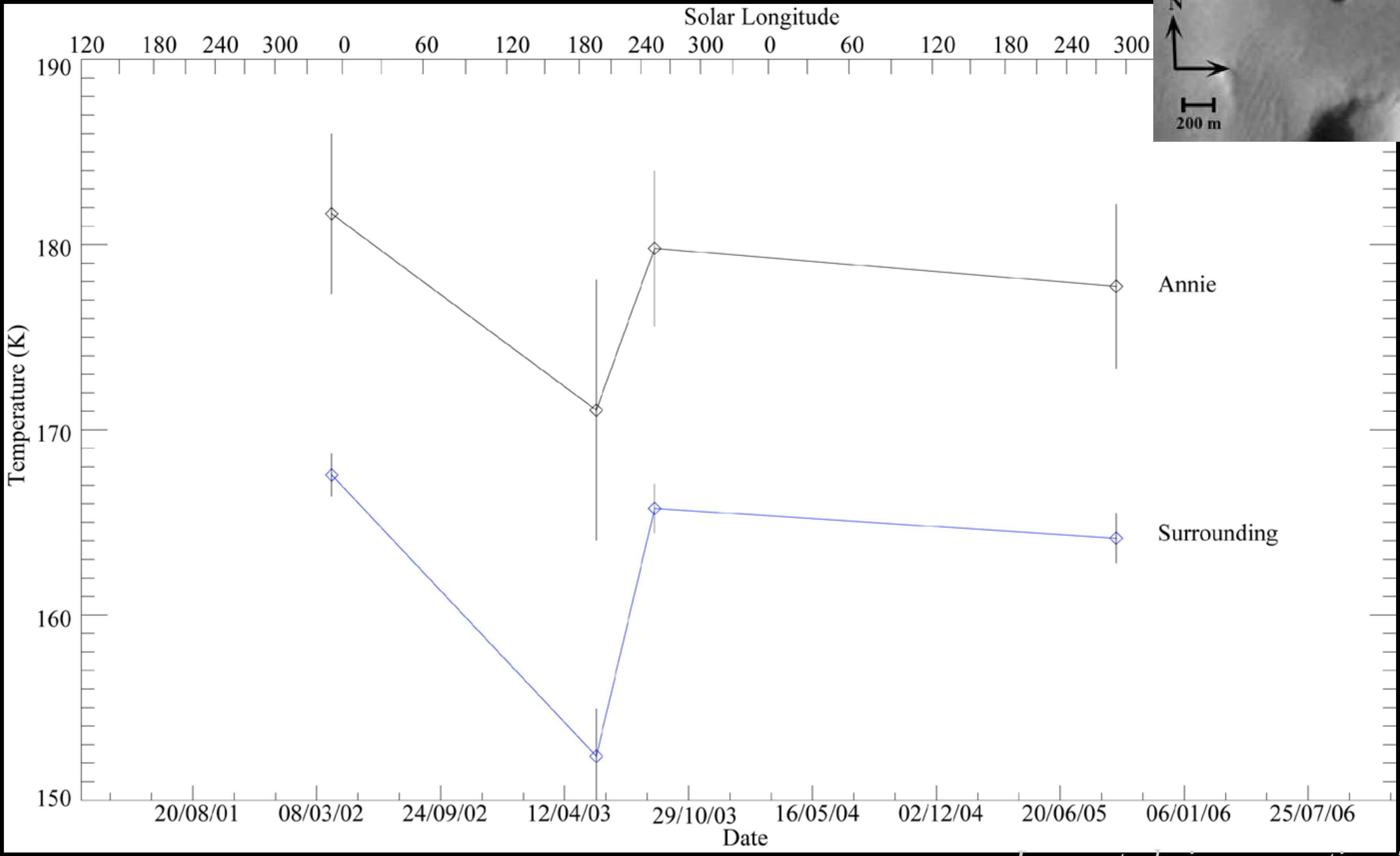

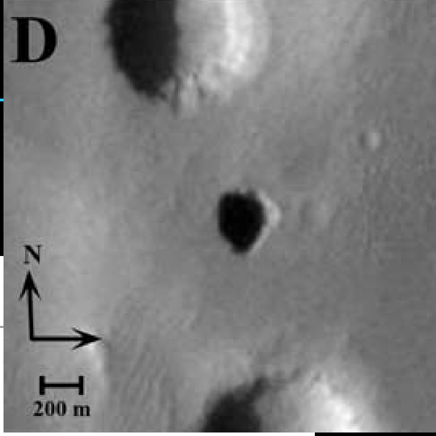

Lopez et al., in preparation, 2009

Thermal behaviour of Dena

Plot of the thermal pattern at different acquisition date. Right corner extract from a THEMIS visible image.

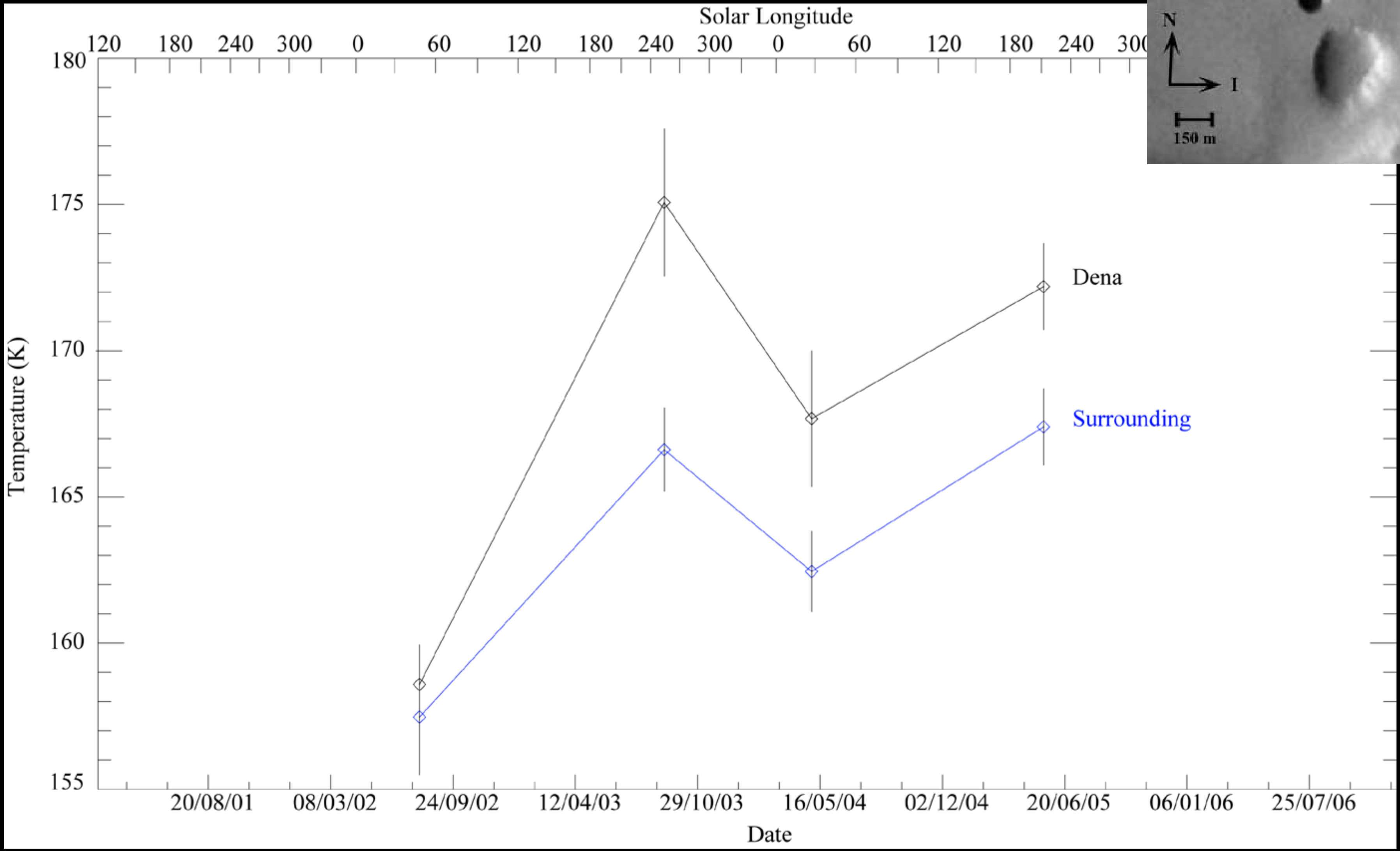

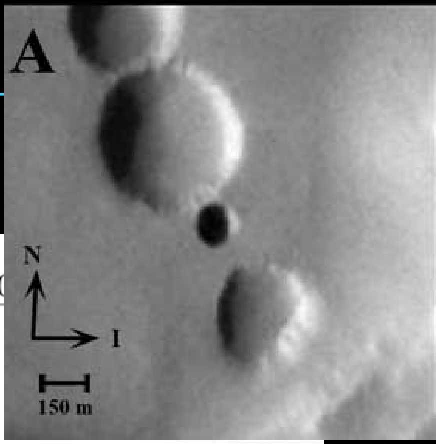

Lopez et al., in preparation, 2009

Influence of the geometry?

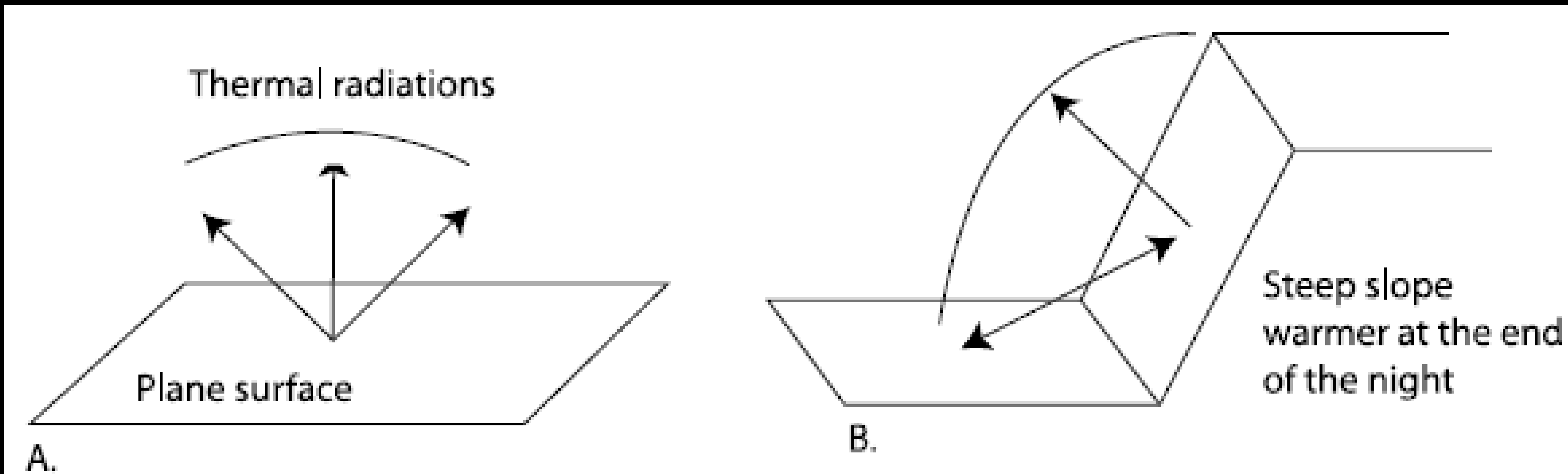

Topographic influence on cooling during night (Baratoux et al, 2005)

Case B, the cooling is less efficient during night.

THEMIS sub-pixels modeling

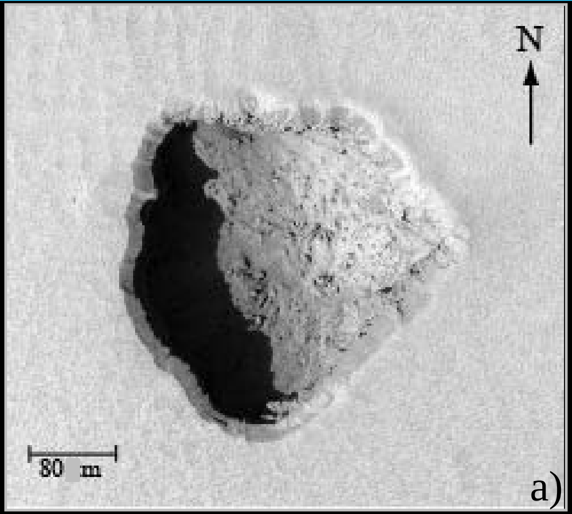

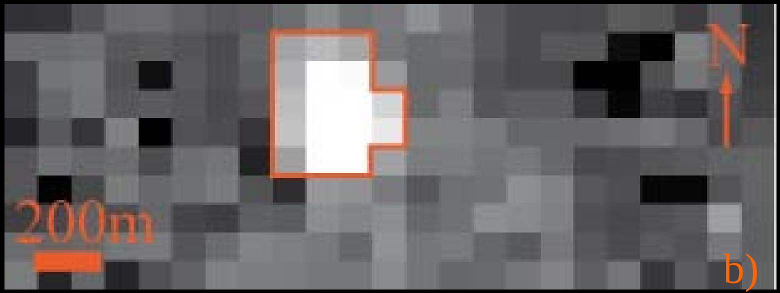

a) HiRISE image extract of pits.

b) Infrared nightime image extract with the limits of hot pixels associated at pits

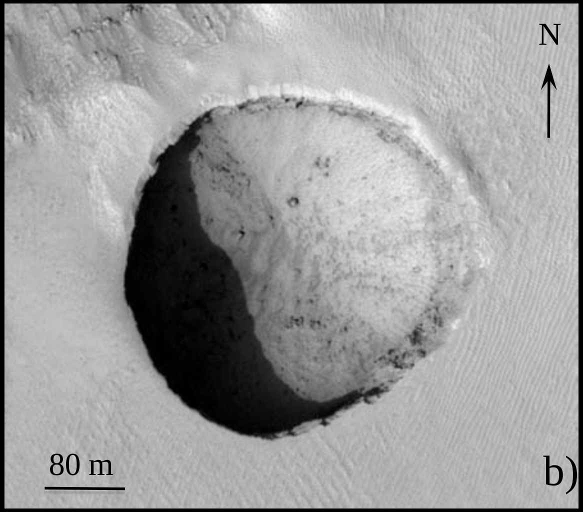

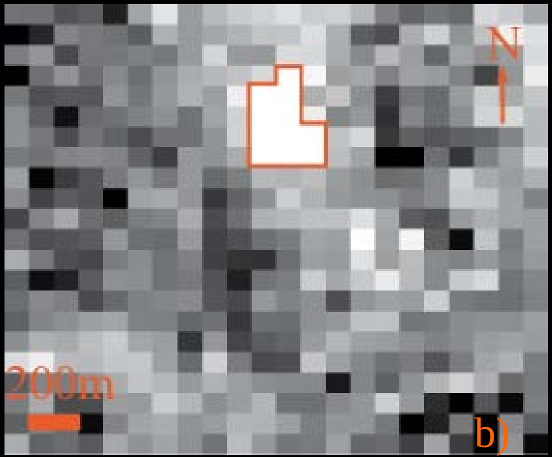

Hot pixels seems to exceeds the pits entrance. To confirm this observation, a thermal model tacking account sub-pixels temperature heterogeneity have been developed

Lopez et al., in preparation, 2009

THEMIS sub-pixels modeling

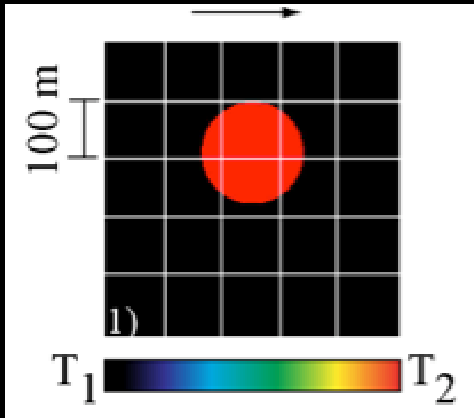

T1 and T2 > pit and background temperature.

White grid > THEMIS spatial resolution. Displaced with an offset from 0 to 1 pixel.

Blackbody law applied to each pixel with two different temperature:

$$\int_{\lambda 1}^{\lambda 2} B(\lambda,T_{eff})\, f(\lambda)d\lambda = p1 \int_{\lambda 1}^{\lambda 2} B(\lambda,T_1)\, f(\lambda)d\lambda + p2 \int_{\lambda 1}^{\lambda 2} B(\lambda,T_2)\, f(\lambda)d\lambda$$

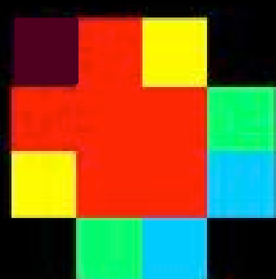

2)

Representation of the effective temperature at THEMIS resolution.

Model warmer surface exceeds the pit entrance

Lopez et al., in preparation, 2009

Results

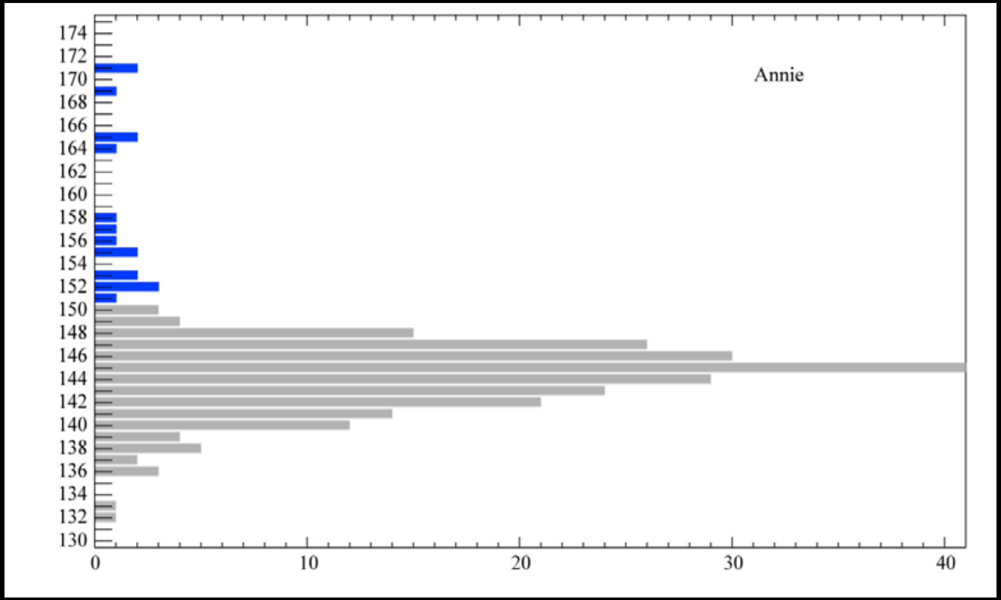

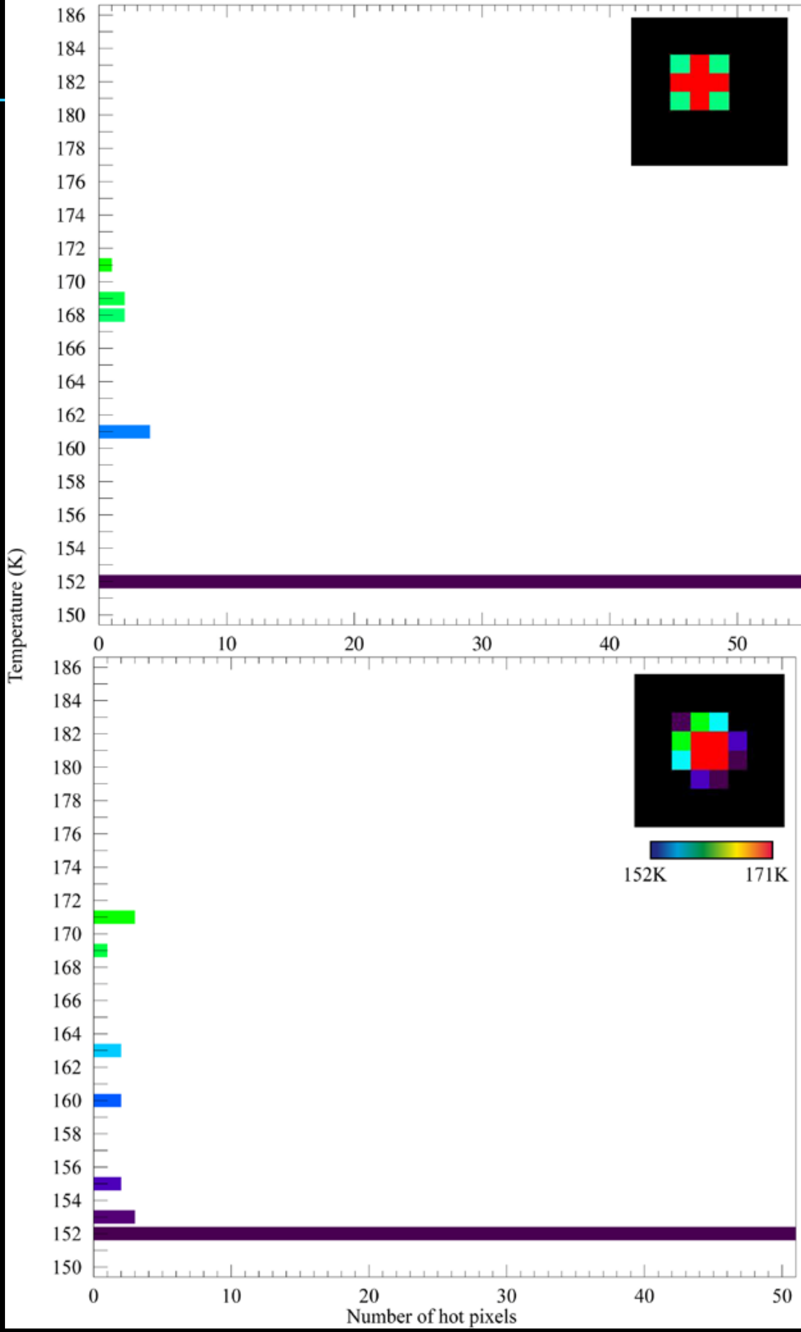

➢Observations : 17 hot pixels
➢Prediction assuming that the warm surface equal that of the sky hole : 9 hot pixel - 13 hot pixels

Lopez et al., in preparation, 2009

Results

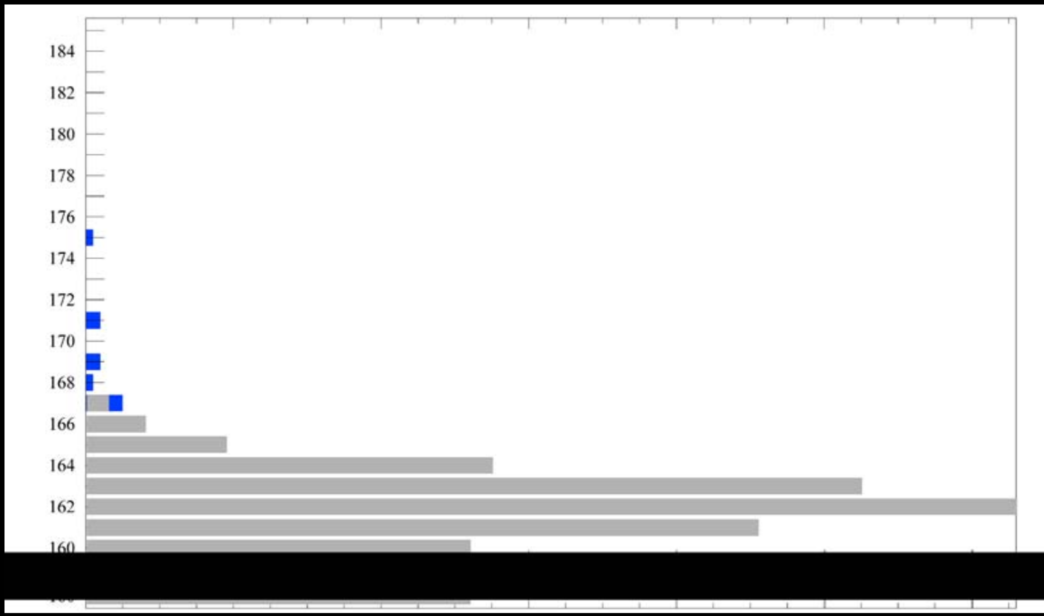

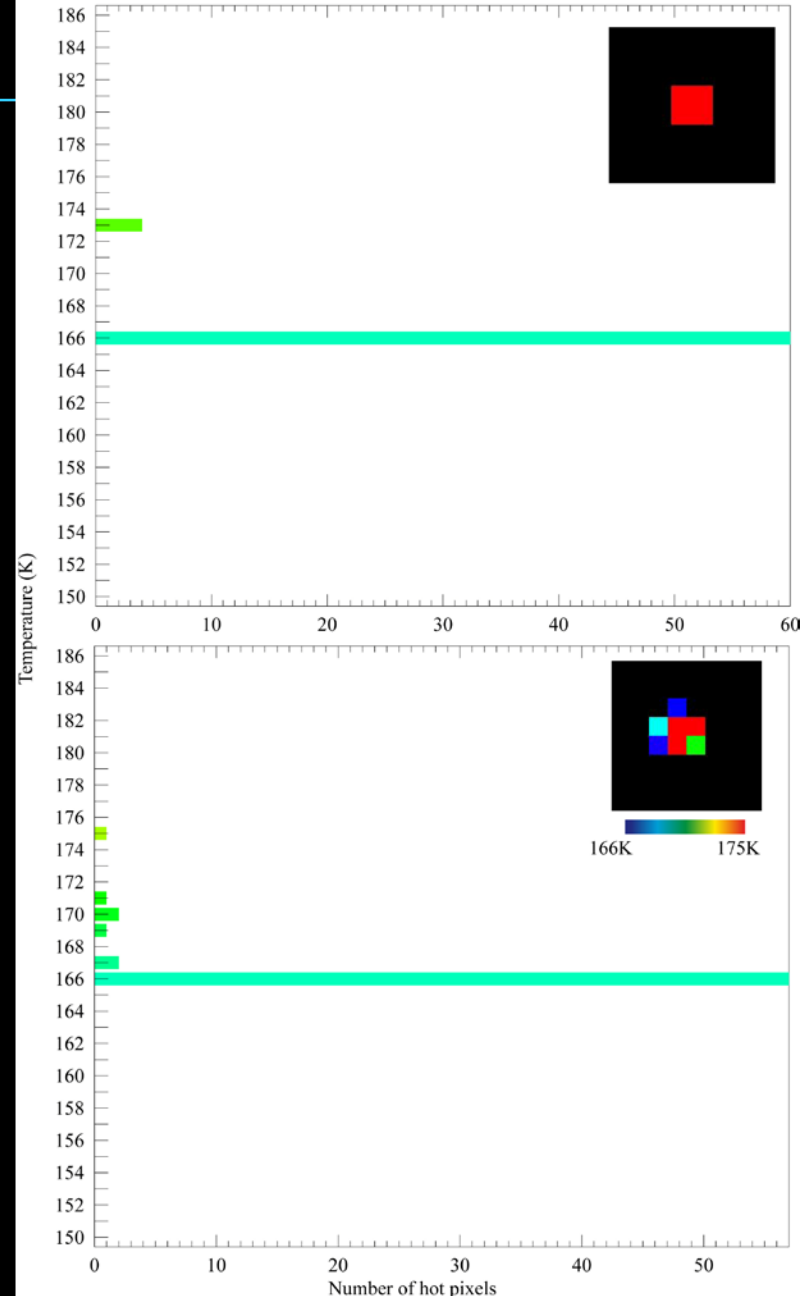

➢Observations : 11 hot pixels

➢Prediction assuming that the warm surface equal that of the sky hole : 4 hot pixel - 7 hot pixels

Comparison between model predictions and observations confirm that the warmer area exceeds the pit entrance. CO_2 convection can explain this observation.

Lopez et al., in preparation, 2009

Pits distribution

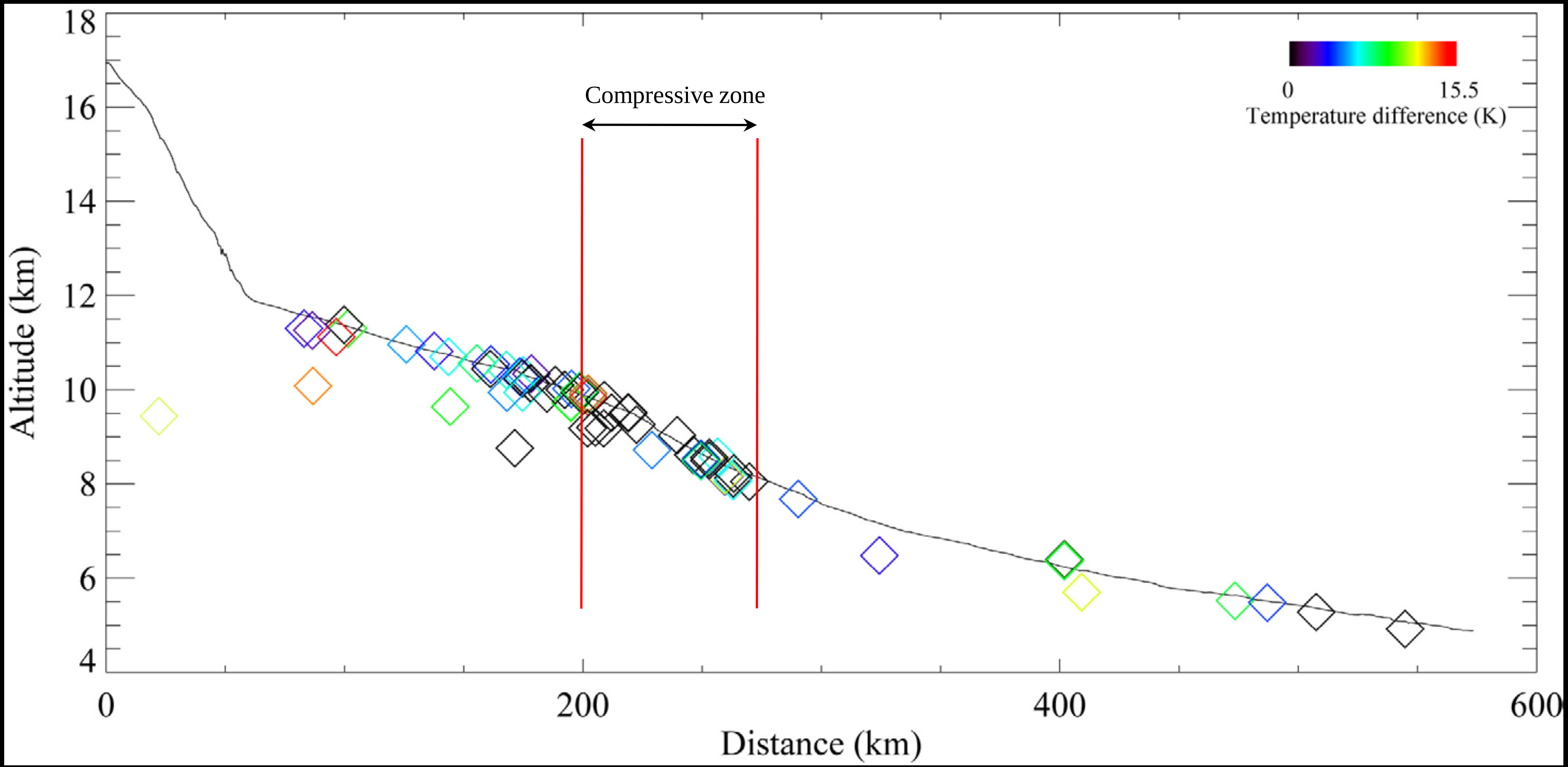

Location of pits across the topographic profile on the South flank. Colors are the ΔT between pits and surrounding.

In the compressive zone (slope break), most of the pits have a ΔT < 5K.

Lopez et al., in preparation, 2009

Thermal pattern of sinuous rilles

Thermal image of one sinuous rille located in the South flank. Temperature and topographic profiles across the sinuous rille.

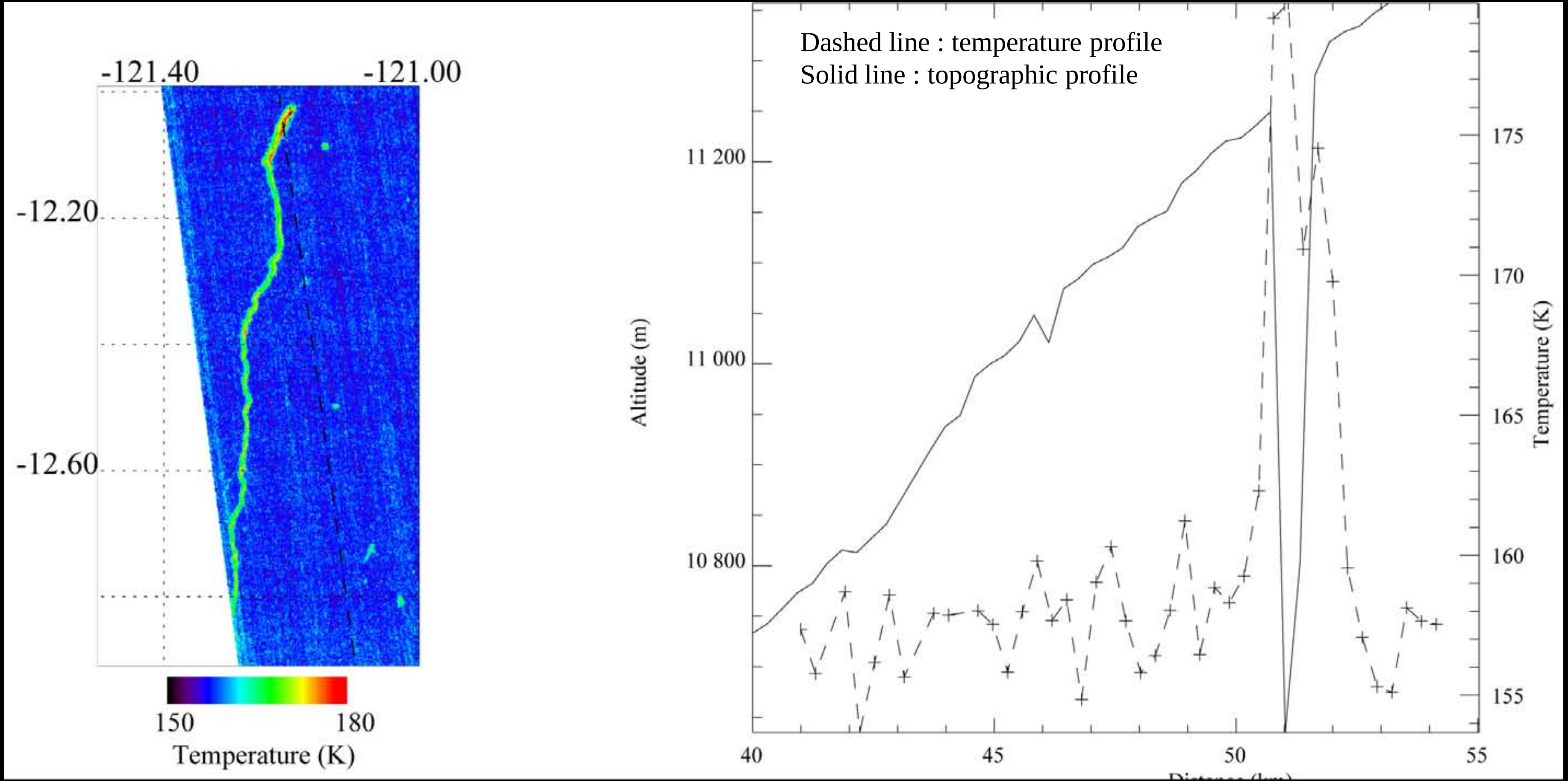

Geometry of the sinuous rille> Length : 56 km, depth : 600 m, wide ≈ 965 m

Lopez et al., in preparation, 2009

Thermal pattern of sinuous rilles

Thermal image of one sinuous rill located in the South flank. Temperature and topographic profiles across the sinuous rille.

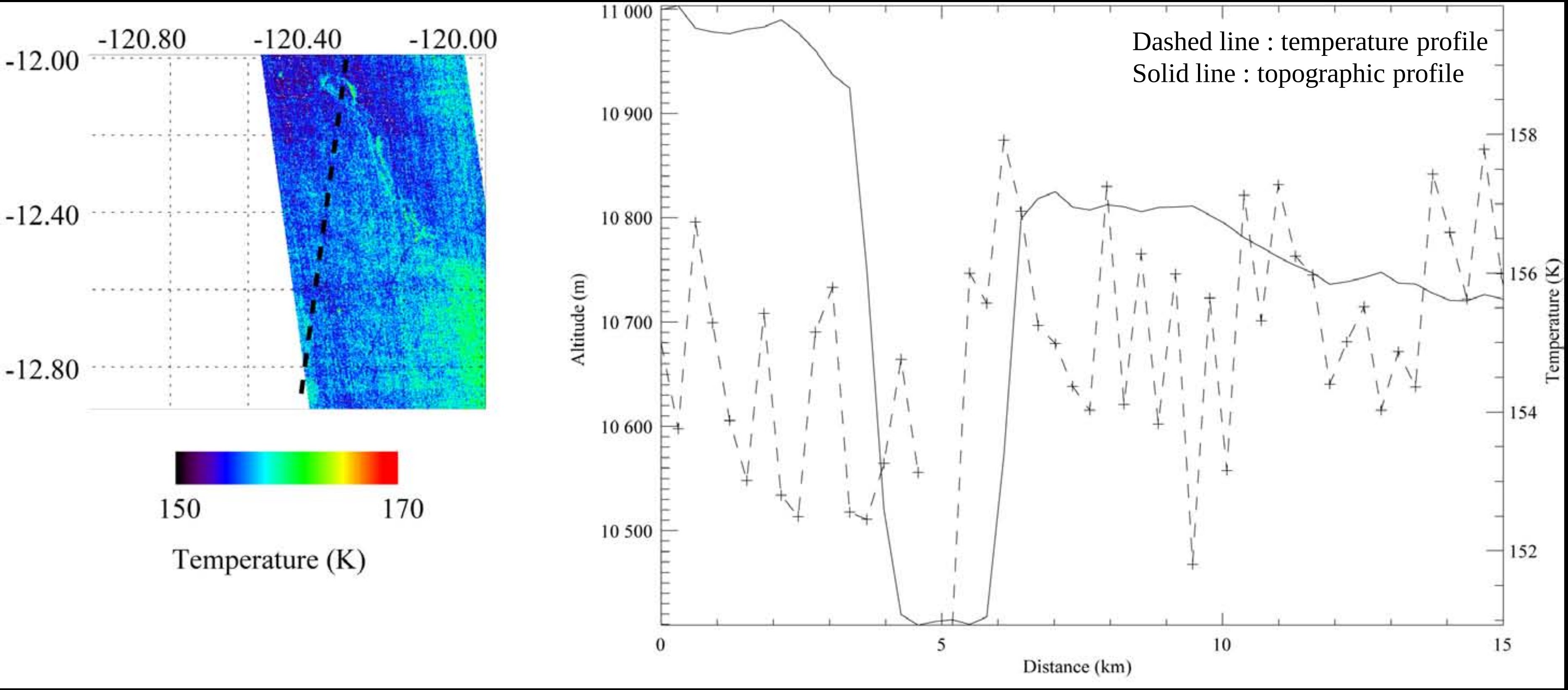

Geometry of the sinuous rille> Length : 36.5 km, depth : 520 m, wide ≈ 3 km

Sinuous rilles have also a thermal pattern which can not be only explained by their shapes.

Lopez et al., in preparation, 2009

2D Numerical model

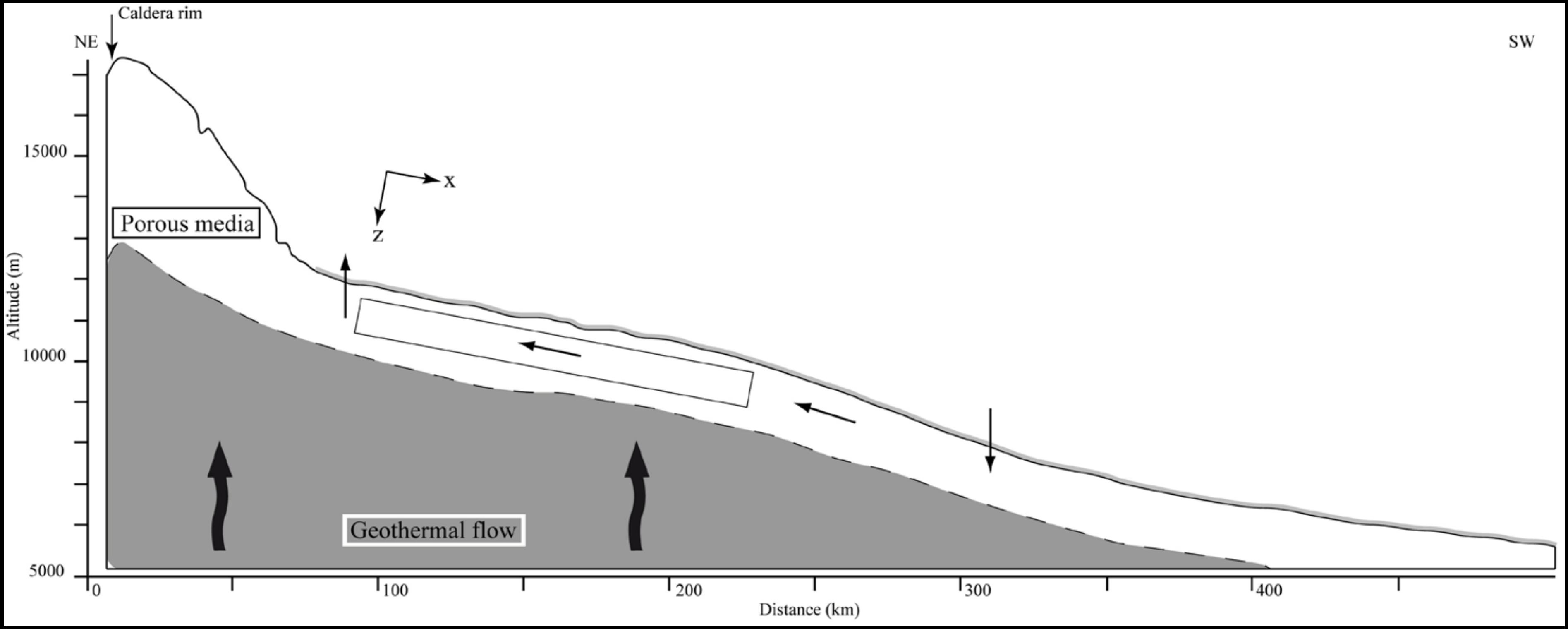

Representation of the box used for the air convection model.

Lopez et al., in preparation, 2009

Preliminary conclusions

- Pits formation : on an extensive region (rift zone), formed by the roof collapse of lava tubes.
- Temperature differences always observed during night, independently of seasons
- Radiative effects can not explain the pits thermal pattern.
- CO_2 convection is the best candidate for explaining the thermal behaviour.
- Other arguments for this hypothesis : warm sinuous rilles and correlation between the pits temperature and compressive region .
- Aerothermal system at the scale of Arsia Mons can exist and could explain the observed thermal pattern.

Conclusion

In Earth, aerothermal system was first observed in a volcanic soils where permeability is very high. First results on Mars shows that this aerothermal system is also possible.

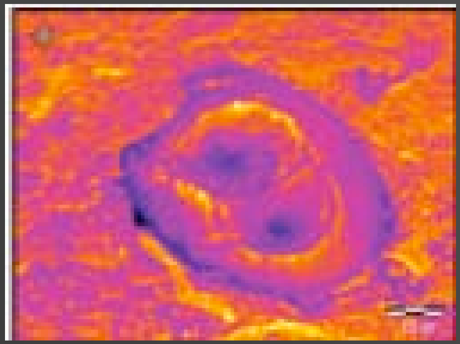

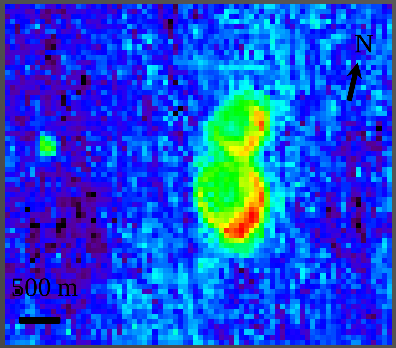

In Mars:

- Cerberus Fossae is a young volcanic plain where thermal pattern can be explain by a CO^2 convection. This convection is enough vigorous to transport an important amount of heat, only possible where permeability is high.
- In Arsia Mons, pits thermal behaviour :

Are always observed (independently of season)

The geometric radiative effects can not explain the observations.

Pits seems to be warmer where extension is observed. It creates an area where vertical permeability is high, making easier the exit of the warm air.

Remaining questions:

- size of the convective cells (local and/or global volcano scale),
- indirect measurement of geothermal heat flow,
- search for the presence of alteration within a pit (data CRISM).

Pits :Common structures on solid planets?

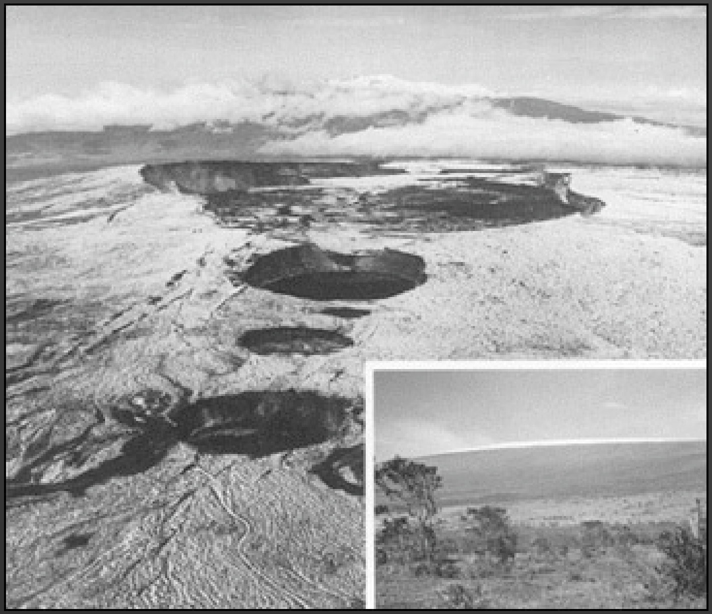

Pits on Earth (Mauna loa)

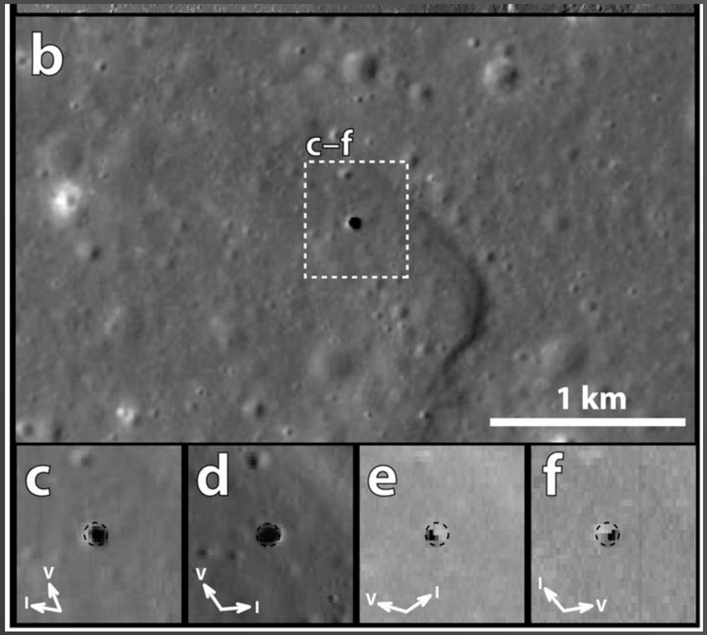

Pit on Moon (Haruyama et al., 2009)

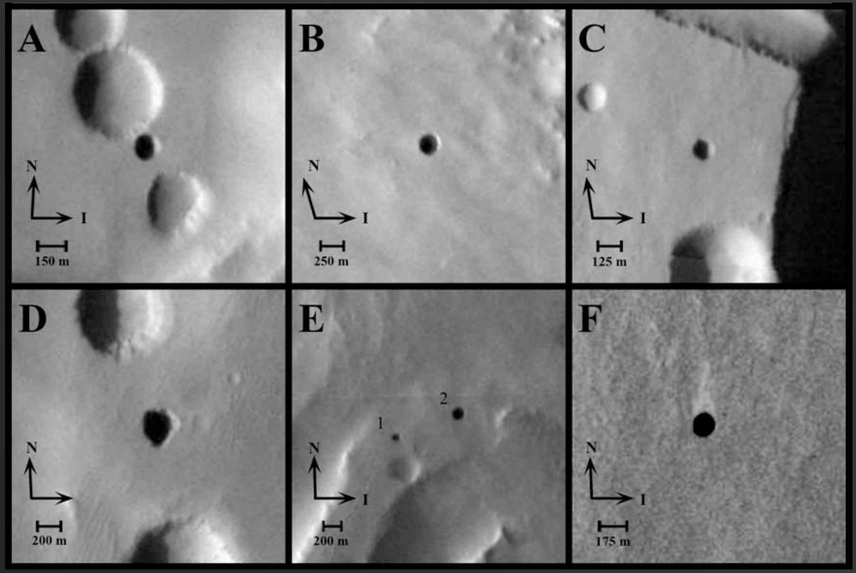

Pits on Mars (Cushing et al., 2007)


Thank you for your attention